

(ALMOST) DARK HI SOURCES IN THE ALFALFA SURVEY: THE INTRIGUING CASE OF HI1232+20

STEVEN JANOWIECKI¹, LUKAS LEISMAN², GYULA JÓZSA^{3,4,5}, JOHN J. SALZER¹, MARTHA P. HAYNES², RICCARDO GIOVANELLI², KATHERINE L. RHODE¹, JOHN M. CANNON⁶, ELIZABETH A. K. ADAMS⁷, AND WILLIAM F. JANESH¹¹ Department of Astronomy, Indiana University, 727 East Third Street, Bloomington, IN 47405, USA; sjanowie@astro.indiana.edu² Center for Radiophysics and Space Research, Space Sciences Building, Cornell University, Ithaca, NY 14853, USA³ SKA South Africa, Radio Astronomy Research Group, 3rd Floor, The Park, Park Road, Pinelands, 7405, South Africa⁴ Rhodes University, Department of Physics and Electronics, Rhodes Centre for Radio Astronomy Techniques & Technologies, P.O. Box 94, Grahamstown, 6140, South Africa⁵ Argelander-Institut für Astronomie, Auf dem Hügel 71, D-53121 Bonn, Germany⁶ Department of Physics & Astronomy, Macalester College, 1600 Grand Avenue, Saint Paul, MN 55105, USA⁷ Netherlands Institute for Radio Astronomy (ASTRON), Postbus 2, 7990 AA, Dwingeloo, The Netherlands

Received 2014 December 23; accepted 2015 February 4; published 2015 March 10

ABSTRACT

We report the discovery and follow-up observations of a system of three objects identified by the ALFALFA extragalactic HI survey, cataloged as (almost) dark extragalactic sources, i.e., extragalactic HI detections with no discernible counterpart in publicly available, wide-field, imaging surveys. We have obtained deep optical imaging with WIYN pODI and HI synthesis maps with WSRT of the HI1232+20 system. The source with the highest HI flux has a newly discovered ultra-low surface brightness (LSB) optical counterpart associated with it, while the other two sources have no detected optical counterparts in our images. Our optical observations show that the detected LSB optical counterpart has a peak surface brightness of ~ 26.4 mag arcsec⁻² in g' , which is exceptionally faint. This source (AGC 229385) has the largest accurately measured HI mass-to-light ratio of an isolated object: $M_{\text{HI}}/L_{g'} = 46 M_{\odot}/L_{\odot}$, and has an HI mass of $7.2 \times 10^8 M_{\odot}$. The other two HI sources (with HI masses 2.0×10^8 and $1.2 \times 10^8 M_{\odot}$) without optical counterparts have upper limit surface brightnesses of 27.9 and 27.8 mag arcsec⁻² in g' , and lower limits on their gas mass-to-light ratio of $M_{\text{HI}}/L_{g'} > 57$ and $> 31 M_{\odot}/L_{\odot}$. This system lies relatively close in projection to the Virgo Cluster, but velocity flow models indicate that it is located at 25 Mpc, substantially beyond Virgo. The system appears to be quite isolated, with no known object closer than ~ 500 kpc. These HI sources may represent both sides of the threshold between “dark” star-less galaxies and galaxies with stellar populations. We discuss a variety of possible formation scenarios for the HI1232+20 system.

Key words: galaxies: formation – galaxies: star formation – radio lines: galaxies

1. INTRODUCTION

Low surface brightness (LSB) galaxies are difficult to detect optically, and thus may be underrepresented in most optically selected samples used in studies of galaxy formation and evolution and their hierarchical assembly history (e.g., Williams et al. 1996; Madau et al. 1998; McGaugh et al. 2000; Brinchmann et al. 2004; Hopkins & Beacom 2006). Some of the LSB galaxies might be those in which star formation has been a slow and gradual process (McGaugh & de Blok 1997; Schombert & McGaugh 2014) and some may provide a source of fresh gas infall to larger galaxies through merger and interactions (Sancisi et al. 1990). By missing the LSB galaxies in most surveys, we may be missing an entire population of galaxies and/or a phase of galaxy evolution.

At the extreme end of the LSB galaxy spectrum, Disney (1976) predicted the existence of entirely “dark galaxies,” with no observable optical stellar counterparts because their surface brightness is too low. A category of “crouching giants,” exemplified by the highly luminous and massive LSB spiral Malin I (e.g., Lelli et al. 2010), has been identified, but they are quite rare. Overall, no large population of unseen LSB objects has been detected at any wavelength.

LSB galaxies typically possess substantial reservoirs of atomic hydrogen, so blind 21 cm surveys represent the best opportunity to find large populations of the most extreme LSBs. Two major blind HI surveys, HIPASS (HI Parkes All Sky Survey; Doyle et al. 2005) and ALFALFA (Arecibo

Legacy Fast ALFA; Haynes et al. 2011), have reached the conclusion that there is not a significant population of gas-bearing but optically dark systems. At the same time, there are a number of intriguing, unexplained objects detected clearly in HI, showing signs of ordered motion and coincident with no discernible stellar counterpart. The best example of such a “dark galaxy” remains the southwestern component of the HI1225+01 system (Chengalur et al. 1995; Matsuoka et al. 2012), although it is important to note its presence in a common envelope with a visible star-forming dwarf companion.

While some simulations can produce dark galaxies in the form of stable gas disks that never produce stars (Verde et al. 2002), others find that star-less galaxies cannot exist for very long before becoming unstable to star formation (Taylor & Webster 2005). The presence of HI in some LSB galaxies provides a key dynamical tracer of the mass in these extreme systems (Geha et al. 2006; Huang et al. 2012a). Detailed kinematic studies are being undertaken to study the effects of outflows and feedback in lower mass galaxies, (van Eymeren et al. 2009), in order to understand star formation modes in these shallow potential wells and low density galaxies. Groups have worked to develop models that can simultaneously explain galaxy scaling relations in the full cosmological context (e.g., Dutton et al. 2007).

Recently, the ALFALFA survey has made significant improvements in the sensitivity and depth of available wide field blind HI surveys. ALFALFA has measured 25,000+ HI sources over 7000 square degrees in a cosmologically significant volume (Giovanelli et al. 2005; Haynes

Table 1
Observed HI Parameters of the HI1232+20 System

AGC	Position J2000	$F_{\text{HI,ALFALFA}}$ (Jy km s ⁻¹)	F_{HI} (Jy km s ⁻¹)	V_{50} (km s ⁻¹)	W_{50} (km s ⁻¹)	R_{HI} ($''$)	$R_5 \times 10^{19}$ ($''$)
(1)	(2)	(3)	(4)	(5)	(6)	(7)	(8)
229385	12:32:10.3 + 20:25:24	4.87 ± 0.04	4.84 ± 0.04	1348 ± 1	34 ± 1	1.60×0.72	1.87×1.10
229384	12:31:36.4 + 20:20:06	1.36 ± 0.03	1.25 ± 0.04	1309 ± 1	27 ± 1	0.73×0.55	1.00×0.70
229383	12:30:55.3 + 20:34:04	0.81 ± 0.06	0.42 ± 0.05	1282 ± 4	59 ± 8	...	0.80×0.28

Note. Observed properties of objects in HI1232+20. (1) Catalog ID in the Arecibo General Catalog (an internal database maintained by M.P.H. and R.G.). (2) HI centroid position from WSRT. (3) Total integrated HI line flux density measured from ALFALFA data. (4) Total integrated HI line flux density measured from WSRT data. (5) Heliocentric velocity, measured at the 50% flux level. (6) HI velocity width, measured at the 50% flux level. (7) HI radius at a HI surface density of $1 M_{\odot} \text{ pc}^{-2}$ (corresponding to an HI column density of $1.25 \times 10^{20} \text{ cm}^{-2}$), in arcminutes, measured from the moment 0 maps assuming a beam of $13'' \times 39''$. Uncertainties on all radius measurements are ± 0.06 . At a distance of 25 Mpc, $1'$ subtends a distance of 7 kpc. Note that AGC 229384 is separated into two peaks at the $1 M_{\odot} \text{ pc}^{-2}$ level, and that AGC 229383 never reaches a surface density of $1 M_{\odot} \text{ pc}^{-2}$. Also note that the measurement for AGC 229383 only reflects the radius of the NW clump; the SE clump reaches a column density of 5×10^{19} over an area of $14'' \times 7''$. (8) HI semimajor and semiminor axis at a column density of $5 \times 10^{19} \text{ cm}^{-2}$, in arcminutes, assuming a beam of $13'' \times 39''$.

et al. 2011; M. Jones et al. 2015, in preparation). ALFALFA has characterized the population of normal galaxies (Huang et al. 2012b), low mass galaxies (Huang et al. 2012a), as well as probing the HI mass function to lower HI masses than ever before (Martin et al. 2010).

As discussed in Cannon et al. (2015), the ALFALFA (Almost) Dark Galaxy Project has been studying the very small fraction ($\sim 0.4\%$) of HI sources which lack obvious optical counterparts and are isolated from other sources. Follow-up observations are ongoing and include deep optical imaging and HI synthesis maps. Many objects turn out to be tidal in origin, but some have very LSB stellar populations at or below the detection limits of current wide field imaging surveys.

In this work we study the newly discovered HI1232+20 system of three (almost) dark extragalactic HI sources which were not detected in optical surveys, and are at least an order of magnitude less luminous than previously studied LSB galaxy populations (e.g., Schombert et al. 2011). This paper is organized as follows. In Section 2 we describe the discovery and observations of this system, and in Section 3 we show the results of those observations. Throughout this work we use a flow model distance (Masters 2005) of $D = 25$ Mpc to the HI1232+20 system, and we discuss the effects of distance uncertainty on our conclusions in Section 3.4.2. In Section 4 we discuss the implications of these objects and what they might mean in the context of (almost) dark galaxies, and in terms of extending scaling relationships from normal galaxies. Section 5 contains a brief summary of our main results. Throughout this work we assume a Λ CDM cosmology, with $\Omega_m = 0.3$, $\Omega_{\Lambda} = 0.7$, and $H_0 = 70 \text{ km s}^{-1} \text{ Mpc}^{-1}$.

2. OBSERVATIONS

2.1. ALFALFA Discovery of the HI1232+20 System

The ALFALFA survey employs a two-pass, fixed azimuth drift scan strategy, the details of which are described in previous papers (Giovanelli et al. 2005; Saintonge 2007; Martin et al. 2009; Haynes et al. 2011). All data are flagged for radio frequency interference interactively, and each grid is examined by hand to confirm and improve on sources detected via the automated methods of Saintonge (2007); final source parameters are measured and cataloged interactively.

Among the ALFALFA (almost) dark extragalactic sources, the HI1232+20 system (comprised of sources AGC 229383, AGC 229384, and AGC 229385) was found to be of particular

interest. These three objects are near each other on the sky and also have similar recession velocities, so are likely associated with each other. From the ALFALFA observations it was clear that these three sources have significant amounts of gas present, even though they do not have readily identifiable optical (stellar) counterparts in existing optical databases (Sloan Digital Sky Survey (SDSS), DSS). While they appear on the sky near AGC 222741 (CGCG 129-006), there is a significant separation in velocity between the sources. AGC 222741 has an HI recession velocity of 1884 km s^{-1} while the three sources in this sample have recession velocities of $\sim 1300 \text{ km s}^{-1}$.

An overlapping archival ultraviolet (UV) image from GALEX GR7 (*Galaxy Evolution Explorer*; Martin et al. 2005; Morrissey et al. 2007; Data Release 7; Bianchi et al. 2014) shows a faint diffuse UV source at the coordinates of AGC229385 (see Section 2.4 for more details). There is also a hint of a faint object at the same position in the DSS2-B image (Digitized Sky Survey⁸) but no source visible at that position in images from SDSS DR9 (Data Release 9; Ahn et al. 2012). Table 1 contains the observed HI parameters of the HI1232+20 system. No optical sources were evident at the locations of the other two HI detections.

Given the curious nature of this system, we have carried out further observations to study it in more detail. We have obtained deep optical images to look for possible faint stellar populations in the sources, and sensitive HI synthesis observations to resolve the gas distribution and kinematics in more detail.

2.2. Deep Optical Imaging with WIYN pODI

The HI1232+20 system was observed with the WIYN⁹ 3.5 m telescope at Kitt Peak National Observatory¹⁰ using the partially populated One Degree Imager (pODI). Currently, pODI is made up of 13 Orthogonal Transfer Arrays (OTAs),

⁸ The Digitized Sky Surveys were produced at the Space Telescope Science Institute under US Government grant NAG W-2166. The images of these surveys are based on photographic data obtained using the Oschin Schmidt Telescope on Palomar Mountain and the UK Schmidt Telescope. The plates were processed into the present compressed digital form with the permission of these institutions.

⁹ The WIYN Observatory is a joint facility of the University of Wisconsin-Madison, Indiana University, the University of Missouri, and the National Optical Astronomy Observatory.

¹⁰ Kitt Peak National Observatory, National Optical Astronomy Observatory, which is operated by the Association of Universities for Research in Astronomy (AURA) under cooperative agreement with the National Science Foundation.

each of which is made of $64\,480 \times 496$ pixel cells. The OTAs are arranged on the focal plane such that the central 3×3 OTAs cover an area of $24' \times 24'$ with pixels that are $0''.11$ on a side. The numerous gaps between cells and OTAs require a series of offset dithered exposures to produce a well-sampled image. Four of the standard SDSS (Gunn et al. 1998; Doi et al. 2010) g' , r' , i' , and z' filters are available, and stars from the SDSS catalog photometry are used for standard photometric calibrations.

We imaged an area which includes both AGC 229384 and AGC 229385 on the night of 2013 February 6 with nine dithered 300 s exposures in each of the $g'r'i'$ filters. We observed AGC 229383 on 2014 May 2 with nine dithered 300 s exposures in both the g' and r' filters. By combining data from these two nights of observations, we have contiguous deep multi-wavelength imaging coverage over an area $\sim 40' \times 40'$. We also imaged this field with an $80\,\text{\AA}$ narrow-band $H\alpha$ filter during photometric conditions on the night of 2013 February 6. Our dithered sequence of nine 300 s images, while not calibrated, do not show any $H\alpha$ detections at the locations of the three HI sources in the HI1232+20 system, but do show a background spiral galaxy (AGC 222741) quite clearly.

We reduced our observations using the QuickReduce (QR; Kotulla 2014) data reduction pipeline, and supplemented this processing with an additional illumination correction. QR was run interactively in the One Degree Imager Pipeline, Portal, and Archive (ODI-PPA)¹¹ science gateway (Young et al. 2013; Gopu et al. 2014). The PPA interface allows the user to select which observations will be reduced, and runs all of the reductions on computing resources at the Pervasive Technology Institute (PTI) at Indiana University.

The QR pipeline includes: masking of saturated pixels, crosstalk, and persistence; overscan subtraction; bias level subtraction; dark current subtraction; nonlinearity corrections to each cell; flat field correction from dome flat fields; cosmic-ray removal; fringe removal (in i'); pupil ghost correction. However, the final pipeline-processed data still have uncorrected instrumental artifacts in them, especially at very faint intensity levels. In order to produce images that are suitable for LSB analysis, we need to correct for the small gradients, sky level offsets, and other artifacts in particular cells. Once these effects are corrected, the dithered images can be combined into a final deep image.

In order to remove these image artifacts, we apply an illumination correction using dark sky flats generated from the observations themselves. For a particular filter, we mask all objects in the images, then use a median algorithm to combine all of the exposures into a dark sky flat field, which is then smoothed with a 3×3 pixel smoothing element. Each exposure is then divided by this illumination correction image.

Before combining all exposures in a dither pattern, we re-project them to a common pixel scale and also scale the images to a common flux level using measurements of stars in the field and SDSS DR9 catalog magnitudes (Ahn et al. 2012). This compensates for varying sky transparency during the dither sequence, and typically yields final photometric zeropoints with standard deviations of 0.02–0.03 magnitudes. The g' filter calibrations required a $g'-i'$ color term of amplitude 0.079

± 0.013 , but r' and i' calibrations required no color term. The point sources in our final combined images have an average FWHM of $0''.7 - 0''.9$.

We also create a deep “detection-only” image by combining all images from both pointings in all filters to reach the faintest light possible. This detection image is then binned to $1/2$ resolution to bring out very faint emission, and is shown in Figure 1 with relevant HI sources labeled and HI synthesis contours overlaid. The contrast levels in this image have been stretched to show the exquisite sensitivity to faint light. In this view, the optical counterpart to AGC 229385 is strikingly visible, as will later be discussed. Also visible in the upper left corner of the image is diffuse filamentary emission from Galactic cirrus. This foreground emission comes from reflections of star light off cold dust clouds in our Galaxy (Sandage 1976; Witt et al. 2008). Multiple infrared surveys (*IRAS*; Schlegel et al. 1998; *WISE*; Wright et al. 2010) also observe this dust via its thermal emission, and show features that are coincident with the faint optical emission we see in our image. It even shows up weakly in the overlapping deep archival *GALEX* UV image. Galactic cirrus is very faint and diffuse at optical wavelengths and typically only visible in deep, wide field images that are very accurately flat fielded (e.g., Rudick et al. 2010).

2.3. HI Synthesis Imaging with WSRT

We observed the HI1232+20 system with four 12 h pointings at the Westerbork Synthesis Radio Telescope (WSRT), three of which were centered on (12:31:52.6 + 20:22:59) to encompass the centroids of AGC 229385 and AGC 229384, and one of which was centered on (12:31:08.5 + 20:31:41.9), to encompass AGC 229383. The primary beams of the two pointing centers are $35'$ wide and cover nearly all of the area displayed in Figure 1. We observed the HI line in one band with 10 MHz bandwidth, two polarization products, and 1024 channels, ensuring a broad range of line free channels for continuum subtraction and a velocity resolution of $4.12\,\text{km s}^{-1}$ after Hanning smoothing.

The data were reduced using the same automated data reduction pipeline as applied in Wang et al. (2013), originally used by Serra et al. (2012), using the data reduction software Miriad (Sault et al. 1995) wrapped into a Python script. The data were automatically flagged for radio interference using a clipping method after filtering the data in both the frequency- and time-domain. After the primary bandpass calibration, the data were iteratively deconvolved with the CLEAN algorithm, using clean masks determined on the cube with decreasing clip levels, to then apply a self-calibration. The calibration solution was applied to the visibilities and the continuum was subtracted in the visibility domain to then invert the data after Hanning smoothing, using a set of combinations of robust weighting and tapering with a Gaussian kernel, as well as a binning in the frequency domain. Finally the data cubes were iteratively cleaned using clean masks determined by filtering the data cubes with Gaussian kernels and applying a clip level. The clean cutoff level was set to the rms noise in the data cubes. Because we cleaned the data comparably deeply, no correction of the intensity levels of the residuals was made.

Our pipeline produces cubes at each centroid with three different robustness weightings, $r = 0.0$, $r = 0.4$, and $r = 6.0$, binned to a velocity resolution of $6.2\,\text{km s}^{-1}$ after Hanning smoothing ($12.4\,\text{km s}^{-1}$ for the $r = 6.0$ cube). The noise level

¹¹ The ODI Pipeline, Portal, and Archive (ODI-PPA) is a joint development project of the WIYN Consortium, Inc., in partnership with Indiana University’s Pervasive Technology Institute (PTI) and with the National Optical Astronomy Observatory Science Data Management (NOAO SDM) Program.

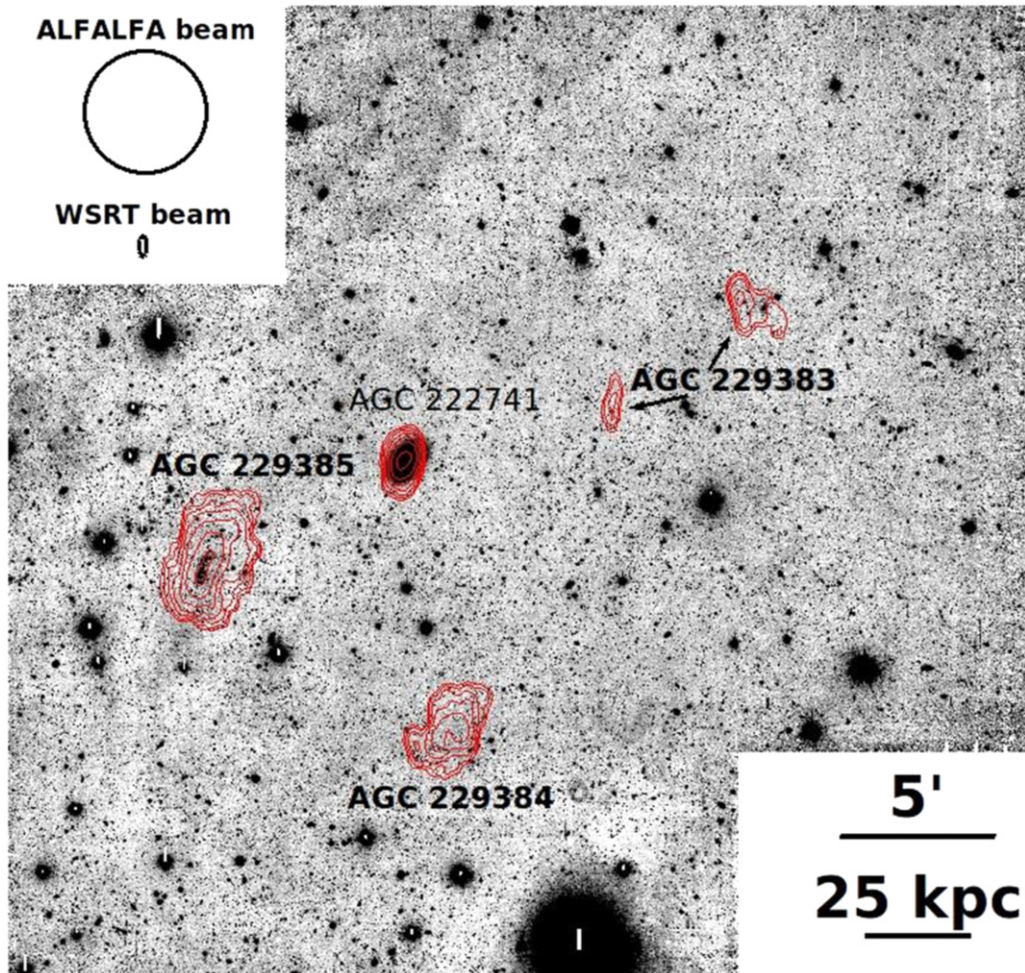


Figure 1. Detection image made from all pODI observations with ALFALFA HI sources in the HI1232+20 system labeled and WSRT contours overlaid in red. The size of the ALFALFA and WSRT beams are indicated by the shapes at the top left corner. The WSRT pointings cover nearly the entire area region shown in this image. The optical image is binned 12×12 pixels so that the resulting pixels are $1''.3$ on a side, and is aligned north up, east left. The WSRT contours show column densities spaced logarithmically between 1 and $64 \times 10^{19} \text{ cm}^{-2}$. The tight packing of the lowest contours is likely a result of sigma-clipping, and not a sharp edge in the HI distribution. See Section 2.3 for more details and about sensitivity differences across the image. The spiral galaxy AGC 222741 has a recession velocity of $cz = 1884 \text{ km s}^{-1}$, so is significantly more distant than the objects in the HI1232+20 system, which have recession velocities around $cz \sim 1300 \text{ km s}^{-1}$ (see Section 3.4.2 for details). The WSRT contours of AGC 229383 show that it is separated into two components at this sensitivity level, as is discussed further in Section 3.3. Also visible at the top left of the image is diffuse filamentary emission from Galactic cirrus, which coincides with features seen in far-infrared and ultraviolet images of the same area.

in the cubes for the three respective robustness weightings are 0.40, 0.36, and $0.24 \text{ mJy/beam/channel}$, with beam sizes of $39'' \times 13''$, $45'' \times 15''$, and $54'' \times 20''$.

For each cube we then created HI total flux maps by summing masked cubes along the velocity axis. We created the masks by smoothing the images to twice the beam size, and then keeping any pixel 3σ above the noise level. From these we calculate HI column density maps assuming optically thin HI gas such that $N_{\text{HI}} = 1.823 \times 10^{18} \int T_b dv \text{ cm}^{-2}$. Since the final contour map results from the combination of multiple WSRT observations (three at the SE pointing, and one at the NW pointing), the signal-to-noise ratio (S/N) varies across the image and is less sensitive near AGC 229383. The lowest HI contour shown on the images, $1 \times 10^{19} \text{ cm}^{-2}$, corresponds to a less significant detection in the region around AGC 229383 than it does in the region around AGC 229385 and AGC 229384. As a result, there were locations outside of the main signal from AGC 229383 where the HI column density exceeded $1 \times 10^{19} \text{ cm}^{-2}$, but since the significance of the detection was $< 3\sigma$, those contours are not shown.

We additionally create a one-dimensional integrated HI line profile for each object, as displayed in Section 3. We fitted the line with both the two-horned function applied in the ALFALFA data processing, and using a standard Gaussian fit and note that the fluxes from the fits match well within random errors. We recover 99% of the ALFALFA flux in the WSRT spectrum of AGC 229385, and 92% in AGC 229384, but only 52% in AGC 229383. The spectra for AGC 229385 and AGC 229384 are both well fitted by a Gaussian profile, and though both may show slight deviation from Gaussian, using two Gaussians does not return a better result. The spectrum for AGC 229383 is not well fitted by either a Gaussian or a two-horned fit.

Finally, we produce HI velocity maps using two different methods. We created standard moment 1 maps from cubes masked at 3σ , and additionally fitted Gaussian functions to each individual profile in the datacube using the GIPSY task XGAUFIT. The resulting maps from the two methods are virtually identical, and we show the maps in Section 3.

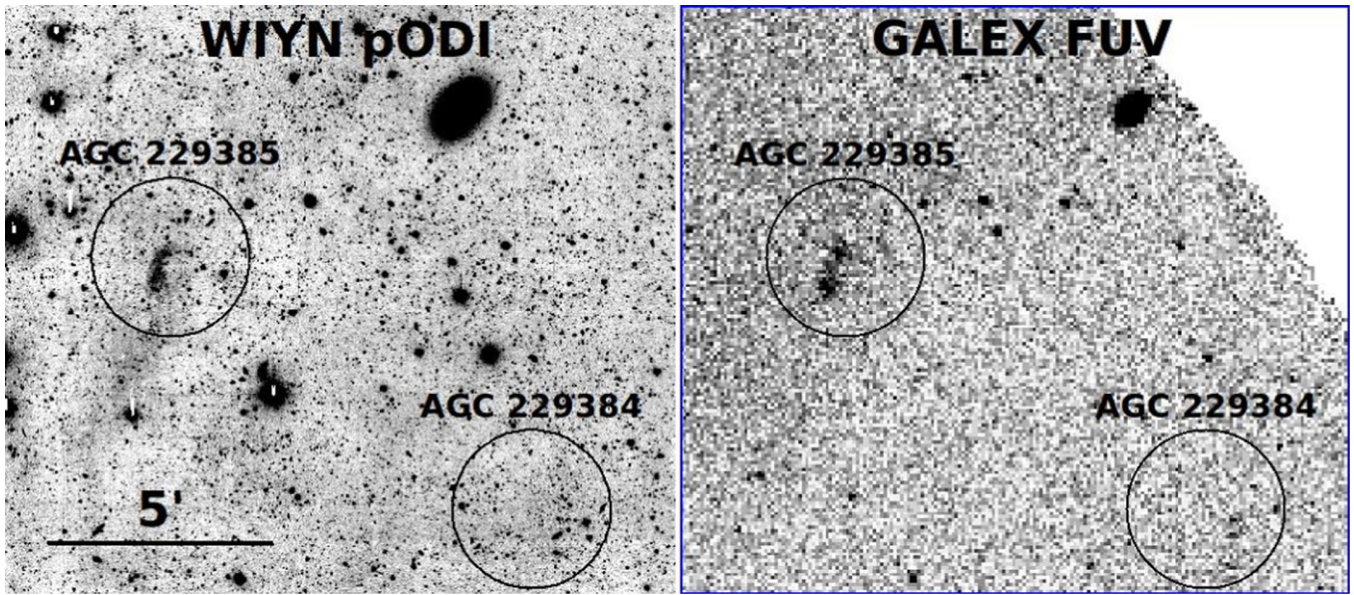


Figure 2. Comparison of WIYN pODI image and *GALEX* FUV image. The pODI detection image is binned 12×12 so that pixels are $1''.3$ on a side. The FUV image has been binned 3×3 so that pixels are $13''$ on a side. Two of the three HI sources in the HI1232+20 system are labeled on both panels with $3''$ circles, the size of the ALFALFA beam. AGC 229385 clearly has an optical and ultraviolet counterpart while AGC 229384 lacks a counterpart at either wavelength. AGC 229383 has not been observed by *GALEX*.

To further analyze the velocity field we create position–velocity (PV) diagrams for each source. We produced the PV diagrams by taking an $18''$ (1 minor axis beam width) wide slice along the HI major axis centered on the HI surface density centroid. We measured the position angle and centroid from the surface density profile since the variations in the velocity field leave the major velocity axis and center uncertain. We note that none of the PV diagrams change significantly for small variations in position angle or slice width.

2.4. Archival *GALEX* Observations

AGC 229385 (the strongest HI detection of the HI1232+20 system) had a very faint UV counterpart visible in an archival dataset from *GALEX* (Martin et al. 2005; Morrissey et al. 2007). *GALEX* obtained images in the far ultra-violet (FUV) from 1344 to 1786 \AA with $4''/3$ FWHM resolution, and in the near ultra-violet (NUV) from 1771 to 2831 \AA with $5''/3$ resolution. These UV images are especially sensitive to young stellar populations, and should help to identify sites of recent star formation.

AGC 229385 was imaged by *GALEX* in 2007 May in the NUV and FUV bands, with exposure times of 1145 s in both bands. A set of matched images is shown in Figure 2, with data from pODI WIYN and *GALEX* FUV. The locations of AGC 229385 and AGC 229384 are shown in these images, while AGC 229383 lies outside of any archival *GALEX* image. The brightest HI source, AGC 229385, is faintly visible in the UV image as a diffuse source. However, the *GALEX* pipeline (GR7; Bianchi et al. 2014) does not identify this diffuse object as a source, instead shredding it into multiple point sources. We measure the brightness of AGC 229385 in the FUV and NUV images ourselves in an aperture matched to our optical images, as discussed in Section 3. There is no source visible in the FUV image at the position of AGC 229384.

3. RESULTS

In the following sub-sections we describe the results of our followup observations for the HI1232+20 system. The derived results are summarized in Table 2. We also consider the environment around this system, and uncertainties in the adopted distance.

3.1. AGC 229385

Figure 3 shows our observations of AGC 229385. Figure 3(a) is a deep three-color image from WIYN pODI with contours from our WSRT HI synthesis map at the highest resolution ($39'' \times 13''$). Figure 3(b) shows a zoomed-in region around the optical counterpart with the regions we use to measure its surface brightness indicated by black squares. The optical emission from AGC 229385 appears very blue, and coincides spatially with the peak of the HI distribution. The optical component appears $\sim 5 \times$ less extended than the radio emission, but both are similarly elongated in the northeast–southwest direction.

AGC 229385 has an unusual optical morphology that is not simple to describe. The optical counterpart is elongated in the N–S direction, but has a nearly constant surface brightness across its entire extent. We fitted an ellipse to the 5σ contour on the g' image and found a semimajor axis of $32''$ and semi-minor axis of $10''$. This 5σ ellipse has a position angle of 15° (measured clockwise from N) and an ellipticity ($\epsilon = 1 - b/a$) of $\epsilon = 0.68$.

After attempts to fit elliptical annuli to the optical images of AGC 229385 resulted in inconsistent and divergent surface brightness profiles, we decided to measure the surface brightness in small regions instead. We measured the optical surface brightness of AGC 229385 in $5'' \times 5''$ regions following the curving shape of this source from south to north, after masking all obvious foreground and background sources. These regions are shown as black boxes in Figure 3(b). We also placed

Table 2
Derived Properties and Limits from Observations

Quantity (units)	AGC 229383	AGC 229384	AGC 229385
$m_{g'}(\text{mag})$	>20.7	>20.7	19.20 (0.03)
$m_{r'}(\text{mag})$	>20.2	>20.5	19.27 (0.03)
$m_{i'}(\text{mag})$...	>19.7	19.36 (0.04)
$\mu_{g',\text{peak}}(\text{mag arcsec}^{-2})$	>27.8	>27.9	26.4 (0.1)
$\mu_{r',\text{peak}}(\text{mag arcsec}^{-2})$	>27.3	>27.7	26.5 (0.1)
$\mu_{i',\text{peak}}(\text{mag arcsec}^{-2})$...	>26.8	26.1 (0.1)
Optical major axes (at $\mu_{g'} = 27$) (kpc)	7×3
HI major axes (at $5 \times 10^{19} \text{ cm}^{-2}$) (kpc)	12×4	14×10	28×16
$M_{g'}(\text{mag})$	> -11.3	> -11.3	-12.89
$M_{r'}(\text{mag})$	> -11.8	> -11.5	-12.79
$M_{i'}(\text{mag})$...	> -12.3	-12.69
$g' - r'(\text{mag})$	-0.09
$B - V(\text{mag})$	0.13
$M_B(\text{mag})$	> -11.2	> -11.1	-12.72
$L_{\text{FUV}}(L_{\odot})$	2.41×10^7
$L_{\text{NUV}}(L_{\odot})$	2.66×10^7
$\text{SFR}_{\text{NUV}}(M_{\odot} \text{ yr}^{-1})$	4.1×10^{-3}
$\text{SFR}_{\text{FUV}}(M_{\odot} \text{ yr}^{-1})$	6.9×10^{-3}
$\log M_{\text{HI}}(\log M_{\odot})$	8.08	8.30	8.86
$M_{\star}(M_{\odot})$	$< 3.7 \times 10^5$	$< 3.4 \times 10^5$	1.5×10^6
M_{HI}/M_{\star}	>320	>580	290
$M_{\text{HI}}/L_{g'}(M_{\odot}/L_{\odot})$	>31	>57	45.8
$M_{\text{HI}}/L_B(M_{\odot}/L_{\odot})$	>26	>48	38.2

Note. Apparent magnitudes ($m_{g'}$, $m_{r'}$, $m_{i'}$) are not corrected for Galactic extinction. Absolute magnitudes ($M_{g'}$, $M_{r'}$, $M_{i'}$, M_B) luminosities (L_{FUV} , L_{NUV}), and colors ($g' - r'$, $B - V$) are corrected for Galactic extinction from Schlafly & Finkbeiner (2011). All absolute quantities assume a distance of 25 Mpc. M_B and $B - V$ are determined from conversions in Jester et al. (2005). Upper limits are determined where sources are not detected in pODI observations and are at 3σ confidence levels. Uncertainties on measured quantities are indicated in parentheses.

similar regions outside the periphery of the source to determine the local sky value. The surface brightness traces along AGC 229385 are plotted in the Figure 3(c). We calculated the surface brightness level that corresponds to three times the standard deviation in the sky, and label it as the 3σ detection threshold. The g' surface brightness profile has the highest S/N, and is well above the 3σ level. The r' profile is weaker but still well-measured. In i' , this source is only weakly detected, but still is above the 3σ surface brightness level. In all three filters a similar profile shape is seen as the outlying regions show very little signal and the inner regions show a relatively flat brightness distribution across the source. To estimate a peak surface brightness value in each filter we use the measurements from the three boxes just south of the bright foreground star near the center of AGC 229385, where there are relatively few contaminating sources which had to be masked and the profiles are relatively smooth. The peak values are calculated by averaging the measurements in these three boxes, and are 26.4, 26.5, and 26.1, in g' , r' , and i' , respectively. While the formal uncertainties on these surface brightness measurements are low

($\sim 3\text{--}5\%$, owing to our accurate photometric calibrations and the good S/N of the optical counterpart), the variations between adjacent boxes can be as high as 0.1 mag. Accordingly, we assign an uncertainty of 0.1 mag to these peak values. We also measure photometry of this source in a $32''$ radius aperture after masking obvious foreground and background sources. The results of the surface and aperture photometry of all three sources are summarized in Table 2.

The HI synthesis observations from WSRT (shown in the bottom row of Figure 3) are also difficult to interpret. The moment 0 map, Figure 3(d), shows an HI source significantly more extended than its optical counterpart. AGC 229385 has HI major and minor axes of $3/2 \times 1/4$ measured at an HI surface density of $1 M_{\odot} \text{ pc}^{-2}$ (corresponding to a column density of $12.5 \times 10^{19} \text{ cm}^{-2}$), or 24×10 kpc assuming a distance of 25 Mpc. WSRT measures significant emission at lower column densities, out to $3/7 \times 2/2$ or 28×16 kpc at $5 \times 10^{19} \text{ cm}^{-2}$ and a furthest extent of $\sim 5'$ at 10^{19} cm^{-2} .

The exact surface density profile of AGC 229385 is subject to its 3D geometry and inclination, which are difficult to determine conclusively given our beam size and the unusual nature of AGC 229385. AGC 229385 appears to have an HI position angle of 21° which gives $\sim 6 \times 7$ resolution elements at the furthest extent along the major and minor axes. We formally measure an inclination of $63 \pm 4^\circ$ assuming a thin HI disk and uncertainties of half the beam size along the major and minor axes.

As an instructive exercise, we assume a disk geometry and compute de-projected surface density profiles for AGC 229385 using Robertson–Lucy deconvolution (Lucy 1974; Warmels 1988; the GIPSY task RADIAL). This method, developed for use in low resolution imaging, works by collapsing the measured intensity along the minor axis, and produces a one-dimensional profile, which is then iteratively matched by a model one-dimensional profile produced by summing axisymmetric, uniform density co-planar rings along lines of sight. This method does not require knowledge of the inclination of the object, but still assumes a disk geometry. The summed one-dimensional surface density profile shows some asymmetry and two peaks with a slight depression in the center. These features are reflected by asymmetry in the resulting RADIAL model, and a strong suggestion of a hole in the center of the HI distribution, a feature that would be smeared out in 2D ellipse fitting analysis. If confirmed, this hole could be indicative of the formation of cold atomic and molecular hydrogen in the center of the object, or of a non-disky, more complicated HI distribution, possibly caused by two recently merged components. However, higher resolution data are necessary to confirm the existence of a gap in the HI distribution.

The HI velocity field of AGC 229385 shown in Figure 3(d) is equally difficult to interpret. The narrow integrated HI line width and single peaked spectrum (shown in Figure 3(f)) is suggestive of slow rotation. If we assume a thermal velocity dispersion of 11.0 km s^{-1} , the 34 km s^{-1} integrated line width of AGC 229385 gives an observed rotation velocity of 16 km s^{-1} when subtracting thermal velocity and dividing by 2. This translates to a rough inclination-corrected rotation velocity of 18 km s^{-1} . Indeed, the moment 1 map shown in Figure 3(d) shows evidence of ordered rotation roughly along the major axis of the source, but the gradient is asymmetric/ The irregular shape of the PV diagram for AGC 229385 (Figure 3(e)) further diagnoses this asymmetry. The southern side of the source

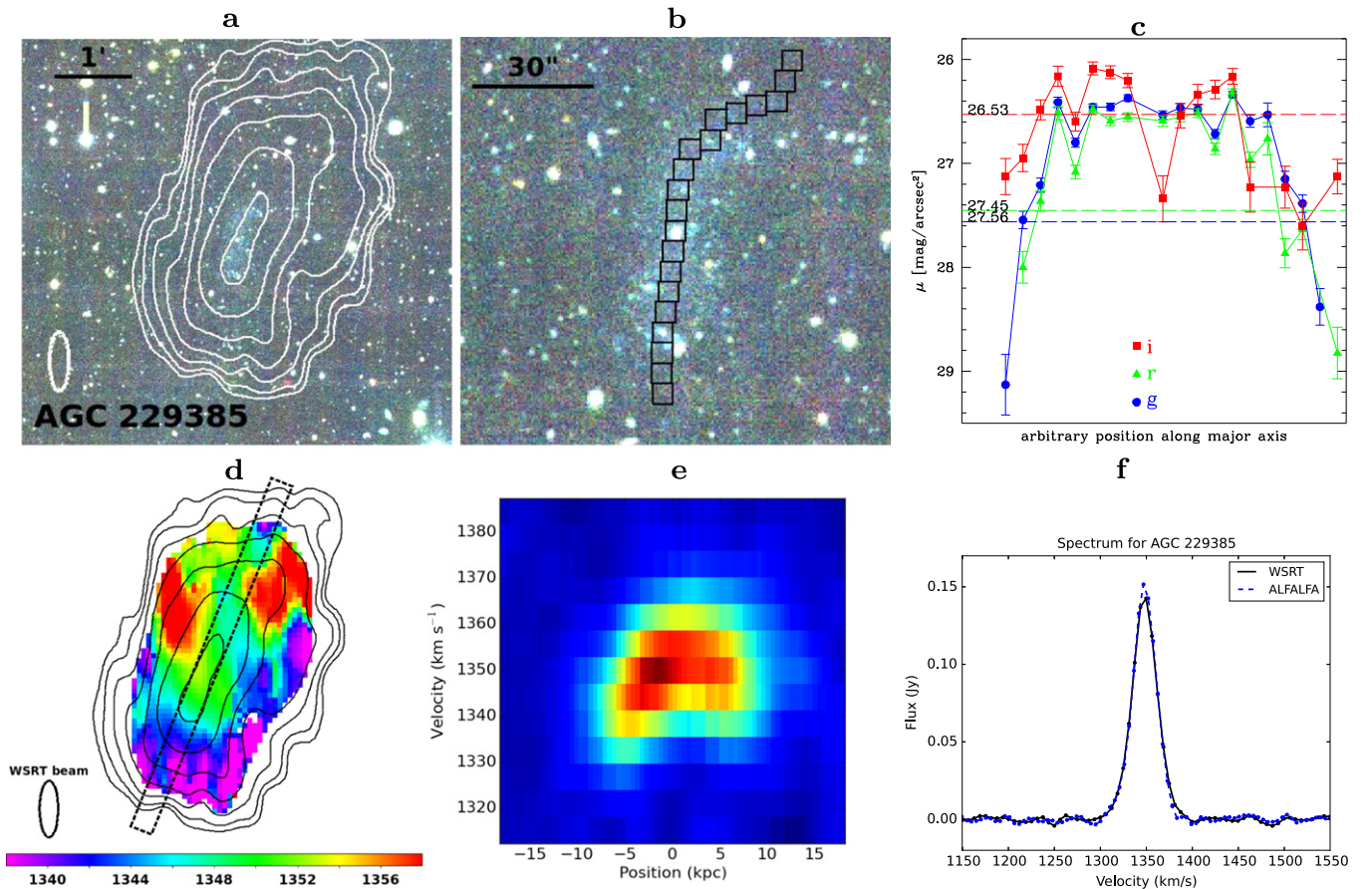


Figure 3. Our observations of AGC 229385. (a) Three-color optical image from WIYN pODI binned 4×4 so that pixels are $0\farcs44$ on a side. North is up, east is left, and the angular scale is indicated on the image. White contours of HI emission are from WSRT and are at $1, 2, 4, 8, 16, 32,$ and 64×10^{19} atoms cm^{-2} , and the white ellipse at the bottom left shows the size and shape of the WSRT beam. (b) Zoomed-in view of the WIYN pODI observations, with black boxes indicating regions used for surface brightness measurements. (c) Surface photometry for AGC 229385 from pODI images in g' , r' , and i' filters, measured in $5'' \times 5''$ boxes following the brightest part of the optical emission, after masking obvious stars and background galaxies. Dashed lines show the 3σ surface brightness detection limits in each filter. Blue points and lines indicate g' filter measurements, green indicate r' measurements, and red indicate i' measurements. (d) XGAUFIT velocity field from WSRT with the same HI contours as above. The ellipse in the bottom left corner indicates the size and shape of the WSRT beam. The dashed rectangular region shows the slice along the major axis which is used to generate the PV diagram. (e) Position–velocity diagram from WSRT. (f) ALFALFA and WSRT HI spectra of AGC 229385. As discussed in the text, HI fluxes from ALFALFA and WSRT are in good agreement. Blue dashed lines represent the ALFALFA spectra, while the solid black lines show the WSRT $r = 0.4$ spectra.

shows a clear slope of $12\text{--}15 \text{ km s}^{-1}$, but then any gradient appears to flatten out or even turn over as one approaches the north side of the galaxy. Further, the PV diagram reveals that the velocity dispersion is of a similar order to the velocity gradient. It is possible that the major axis of rotation is offset from the surface density major axis: fitting a PV diagram at 0° removes any turnover in the north side of the object, but does not give a significant gradient.

The FUV image of AGC 229385 from *GALEX* is shown in Figure 2. While this image is less striking than the optical images, this source is still detected in both the NUV and FUV images. The *GALEX* pipeline shreds this extended source into multiple point sources, so we measure its brightness in the same $32''$ radius aperture and with the same masking that was used on the optical images. The apparent magnitude and uncertainties in the NUV and FUV bands are $19.631 (0.069)$ mag and $19.155 (0.035)$ mag, respectively. After correcting for Galactic extinction, we use the assumed distance of 25 Mpc to determine star formation rates (SFRs) from the NUV and FUV luminosities following the relations of Murphy et al. (2011) and Hao et al. (2011), and report the results in Table 2. We do not include a correction for internal extinction.

Using the flow model distance of 25 Mpc, we derive absolute global parameters for AGC 229385, which are listed in Table 2. AGC 229385 has an optical luminosity comparable to typical dwarf galaxies (converted to $M_B = -12.72$ via Jester et al. 2005). Its $g' - r'$ color is very blue, and corresponds to a $B - V$ color of 0.13 (via similar conversion in Jester et al. 2005). Using this B magnitude instead of the SDSS g' magnitude, we find $M_{\text{HI}}/L_B = 38.2 M_\odot/L_\odot$. Using the self-consistent simple stellar population models discussed in McGaugh & Schombert (2014), this color implies a stellar mass-to-light ratio (in the V -band) of $M_*/L_V = 0.3 M_\odot/L_\odot$, or a total stellar mass of $\sim 1.5 \times 10^6 M_\odot$, and a ratio $f_{\text{HI}} = M_{\text{HI}}/M_* = 475$.

3.2. AGC 229384

Figure 4(a) shows the deep three-color WIYN pODI image of AGC 229384 with WSRT HI contours overlaid. No obvious optical counterpart is visible. The faint grid of horizontal and vertical stripes in the background is an artifact from the data reduction process. Figure 4(b) shows a zoomed-in view near the twin peaks of the HI contours (marked with black “x”s). We used small $5'' \times 5''$ regions placed around this area to

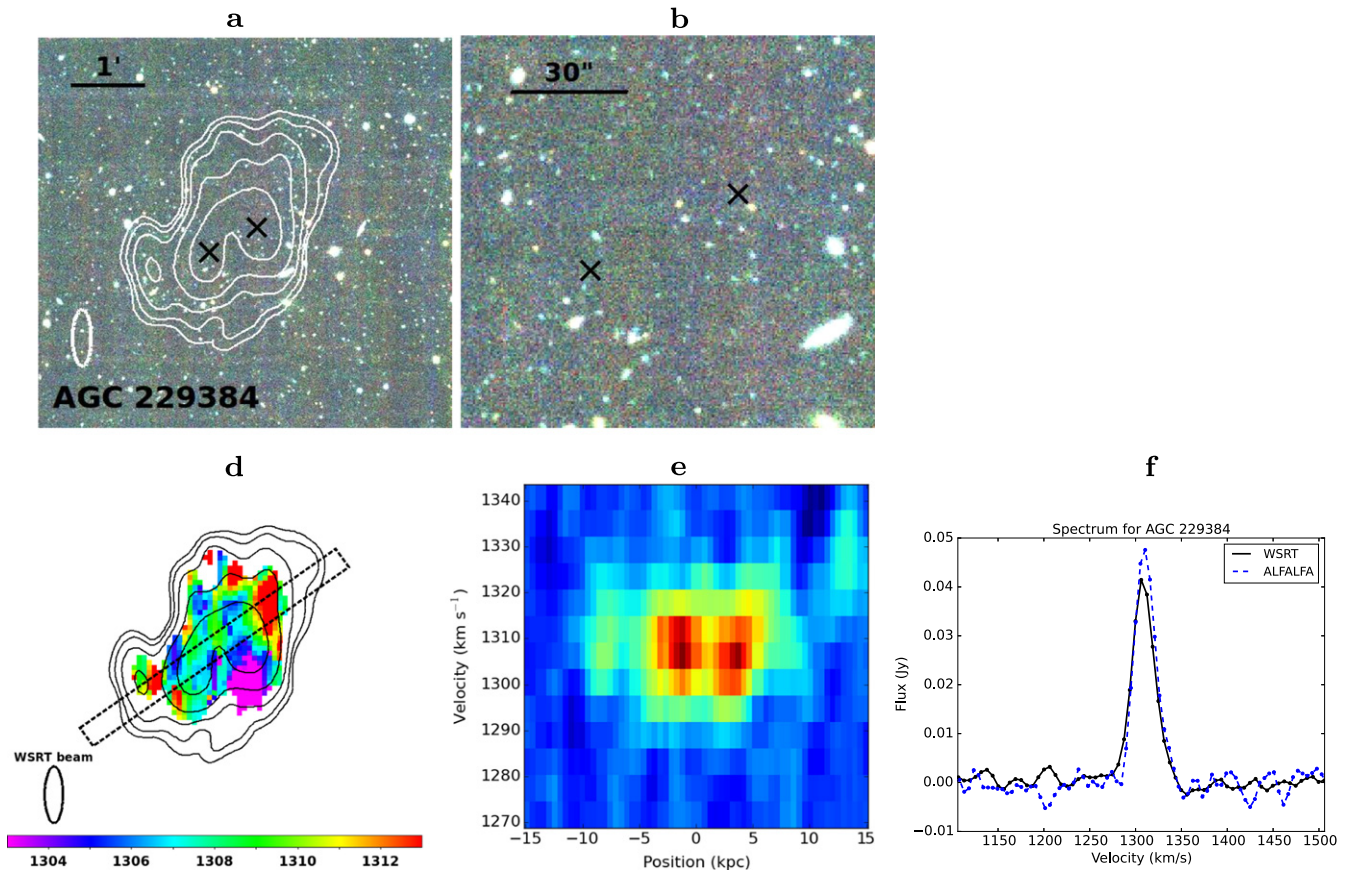


Figure 4. Our observations of AGC 229384, same panels as Figure 3. No optical counterpart is detected down to an upper limit of $\mu_{g'} \sim 27.8$ mag arcsec $^{-2}$, so no surface brightness profiles are shown. The black “x”s in panels (a) and (b) mark the two peaks of the HI distribution. The HI velocity field of AGC 229384 in panel (e) shows no evidence of ordered rotation. As with AGC 229385, the WSRT and HI spectra in panel (f) are in good agreement with each other.

determine upper limits on the optical non-detection, using the same method as for AGC 229385, after masking all obvious foreground and background sources. The 3σ upper limits on this non-detection are given in Table 2, and are 27.9, 27.7, and 26.8 mag arcsec $^{-2}$ in g' , r' , and i' , respectively. To estimate an upper limit on an integrated magnitude, we must assume an aperture size. Since the HI major axis of AGC 229384 is $\sim 50\%$ of the HI major axis of AGC 229385, the aperture is scaled by the same amount, to $15''$. Using this aperture of radius $15''$, we find 3σ upper limits on the integrated magnitude in g' , r' , and i' filters to be 20.7, 20.5, and 19.7 mag, respectively. These upper limits are used to generate upper limits on $M_{\text{HI}}/L_{g'}$, M_* , and M_{HI}/M_* , all of which are shown in Table 2. In particular, these non-detections correspond to a stellar mass upper limit of $M_* < 3.4 \times 10^5 M_\odot$. When necessary, the observed colors of AGC 229385 were used to make filter conversions on the optical non-detections for AGC 229384. An archival *GALEX* image that covers AGC 229384 also shows no optical counterpart for this object (see Figure 2).

The HI contours of AGC 229384 in Figure 4(a) show an irregular distribution with two weak density peaks. The HI major axes at a surface density of $1 M_\odot \text{ pc}^{-2}$ are $1/4 \times 1/2$ or 10×8 kpc. The HI velocity field shown in Figure 4(d) is patchy and irregular, and appears to be dominated by random motions. The PV diagram in Figure 4(e) shows no evidence of ordered rotation. At its assumed distance of 25 Mpc, AGC 229384 has a total HI mass of $M_{\text{HI}} = 2.0 \times 10^8 M_\odot$. Complete details are given in Tables 1 and 2.

3.3. AGC 229383

From the ALFALFA HI observations, AGC 229383 was extracted as a single, possibly extended weak source. Follow up observations with the single pixel *L*-Band Wide (LBW) receiver confirmed the existence and extended nature of the source, since the more sensitive LBW observations only recovered 64% of the original ALFALFA flux, as shown in Figure 5(f). WSRT observations resolve the source into two low HI column density clumps, separated by 5.5 arcmin (~ 40 kpc at $D = 25$ Mpc). The SE clump is only detected in a single beam at low signal to noise ratio, but is detected in both WSRT pointings which overlap its position. It is possible that these two clumps are independent sources. However, the two clumps together only recover 52% of the original ALFALFA flux, suggesting that there may be gas connecting the sources below the sensitivity of the synthesis observations. AGC 229383 may be two distinct sources, but because the missing flux and the clumpy HI distribution are ambiguous as to the true nature of the source, we choose to discuss it as a single source with two peaks in the remainder of this paper.

Figure 5(a) shows the color image made from the g' and r' observations of AGC 229383, which is located $19'$ to the NW of AGC 229385. As with AGC 229384, no optical counterpart is visible. Figure 5(b) shows the zoomed-in region around the NW peak of the HI distribution. Again we masked obvious foreground and background sources and used regions around this area to measure the background statistics and determine upper limits on the optical non-detection using the same method as for AGC 229385. These 3σ upper limits are given in

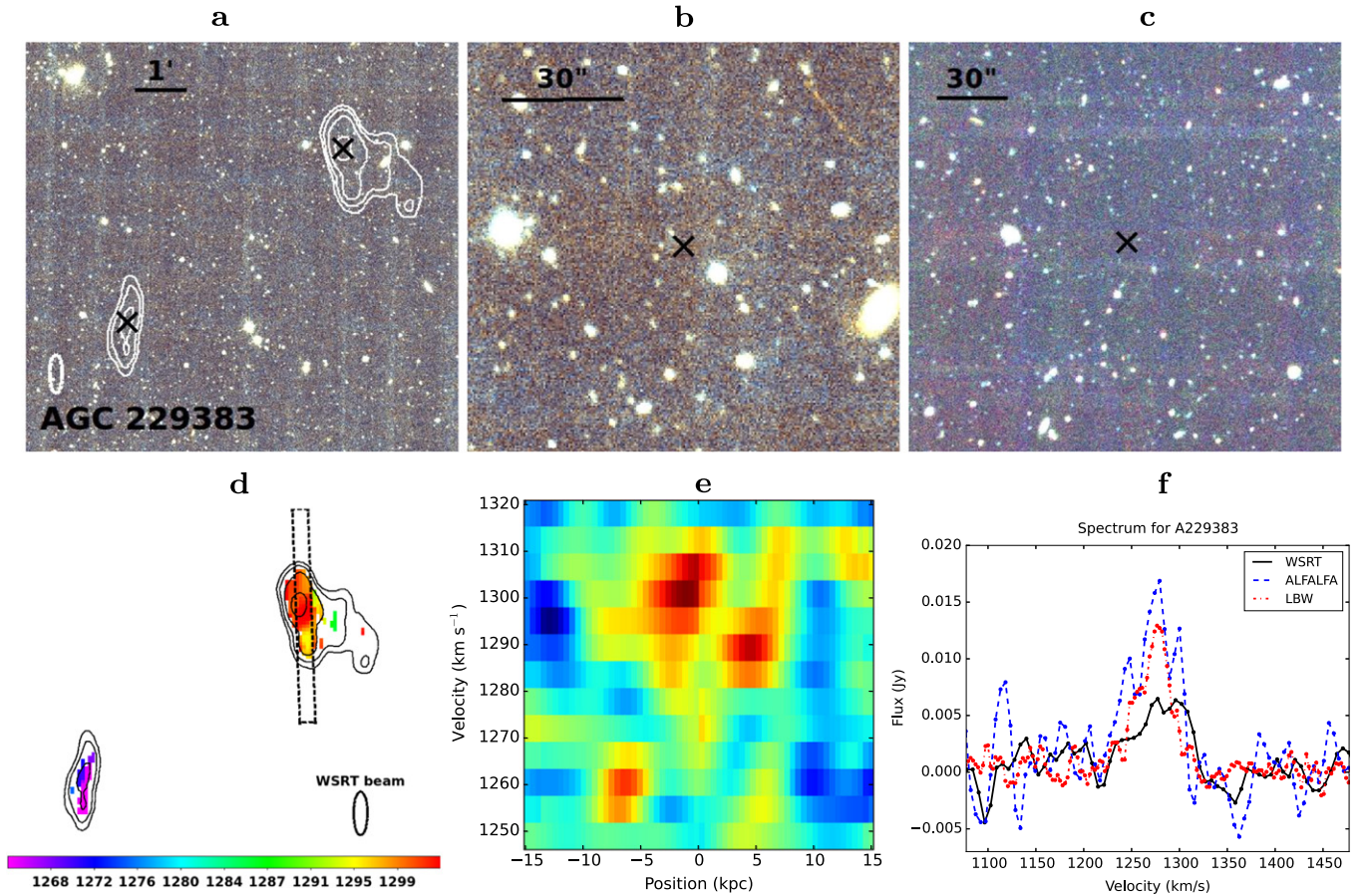


Figure 5. Our observations of AGC 229383, same as Figure 3. (a) WIYN pODI optical image covering both peaks of the HI distribution, with contours from WSRT and black “x”s marking the HI peaks. (b) A zoomed in view of the NW component, with a black “x” marking the peak of the HI distribution. No optical counterpart is detected. An asteroid trail is also visible in this image. (c) A zoomed in view of the unresolved SE component, with its center marked. Again no optical counterpart is detected. (d) The moment 1 map from WSRT with the same HI contours as above. The ellipse in the bottom right corner indicates the size and shape of the WSRT beam. The dashed rectangular region shows the slice along the major axis which is used to generate the PV diagram to the right. (e) Position–velocity diagram from WSRT. No ordered rotation is visible in this splotchy and irregular velocity field. (f) ALFALFA, WSRT, and LBW HI spectra of AGC 229383. As discussed in the text, LBW recovers 64% of the ALFALFA HI flux, and WSRT recovers only 52%. This likely means that there may be extended gas below the WSRT sensitivity which connects these sources, and we consider them to be peaks of a common source in this work.

Table 2, and are 27.8 and 27.3 mag arcsec^{−2}, in g' and r' , respectively. Similarly, we find upper limits on integrated magnitudes in a 15'' aperture of 20.7 and 20.2 mag in g' and r' , respectively. We use these in the same way as AGC 229384 to generate upper limits for the derived quantities for AGC 229383, all of which are listed in Table 2. Figure 5(c) shows the zoomed-in region around the unresolved SE peak of AGC 229383, and reveals no optical counterpart as well.

The HI contours of AGC 229383 in Figure 5(a) show the two density peaks, of which the NW component appears resolved and the SE component unresolved. The HI never reaches a projected HI surface density of $1 M_{\odot} \text{pc}^{-2}$ (corresponding to a column density of $12.5 \times 10^{19} \text{cm}^{-2}$ at this distance), and has a maximum extent of only $48'' \times 17''$ at a column density of $5 \times 10^{19} \text{cm}^{-2}$. The HI velocity field is patchy and irregular, and appears to be dominated by random motions, though our data are limited due to the fact that the two peaks are poorly resolved or unresolved. The limited data and patchy nature of the velocity field precluded meaningful fitting with XGAUFIT, so instead we show the moment 1 map in Figure 5(d), and the messy PV diagram in Figure 5(e). At its assumed distance of 25 Mpc, AGC 229383 has a total HI mass of $1.2 \times 10^8 M_{\odot}$.

3.4. Isolation, Environment, and Distance Uncertainty

3.4.1. Isolation of the HI1232+20 System

Since many “dark” galaxy candidates turn out to be tidal features (e.g., VIRGOHI21; Duc & Bournaud 2008) rather than isolated galaxies, we look for possible objects which may have recently tidally interacted with HI1232+20. To test this possibility, we searched all cataloged nearby sources in the Arecibo General Catalog (AGC), NED, and the SDSS spectroscopic survey and determined the timescale on which they could have interacted with this system, given their current velocities. If we generously assume that a flyby encounter may have had a relative velocity of $\sim 500 \text{ km s}^{-1}$, we can calculate how long ago the nearby objects could have interacted. Naturally, the three sources in the HI1232+20 system all have short interaction time scales with each other ($< 300 \text{ Myr}$, based on these assumptions). The only source with an interaction time scale $< 1 \text{ Gyr}$ is AGC 742390, which is $\sim 30'$ W of this system and has $cz = 1127 \text{ km s}^{-1}$. AGC 742390 is an elongated star-forming galaxy with $M_g = -15 \text{ mag}$, assuming it is at the same distance of 25 Mpc. At this distance, AGC 742390 has a projected separation from the HI1232+20 system of $\sim 200 \text{ kpc}$, but its smaller recession velocity ($\Delta v \sim 200 \text{ km s}^{-1}$) implies that it is likely more nearby than this system. Given the lack of obvious

nearby galaxies in optical and HI surveys, and the lack of objects which could have recently tidally interacted with this system, it seems that HI1232+20 is a locally isolated system, and not a tidal feature of a larger parent object. Still, we cannot exclude the possibility that this system may have been produced as a result of tidal interactions or other gas stripping processes.

3.4.2. Effects of Distance Uncertainty and the Environment

Throughout this work we have adopted a flow-model distance (Masters 2005) of $D = 25$ Mpc to the HI1232+20 system. However, given its location on the outskirts of the Virgo Cluster, there is some uncertainty about its true distance. We consider the possibility that the HI recession velocity may not give an accurate distance for this system, which could affect the derived absolute properties of the objects in the HI1232+20 system.

Large scale peculiar motions have been observed around the Virgo Cluster of galaxies, even beyond its virial radius, due to its significant gravitational influences. Recently, Karachentsev et al. (2014) used a large sample of 1801 galaxies (mostly from Karachentsev & Nasonova (2010) and with some new observations) in the vicinity of the Virgo Cluster which have independent distance measurements (e.g., Tully–Fisher, TRGB, Cepheid) as well as measured recession velocities. This kinematic sample of galaxies was used to map out the zero-velocity surface around the cluster, which encloses the region of space where galaxies are falling into the Virgo Cluster. Karachentsev et al. (2014) find that the zero-velocity surface radius is 7.2 ± 0.7 Mpc, which corresponds to a projected radius of $25^\circ \pm 2^\circ$ at their assumed Virgo distance of $D = 17.0$ Mpc. The HI1232+20 system is at a projected distance of only $\sim 8^\circ$ from the center of the Virgo Cluster (NGC 4486), and may be participating in the infall motion. Figure 1 in Karachentsev & Nasonova (2010) shows a graphical representation of the difficulty in determining distances from recession velocities in this region, and for this system’s measured recession velocity of ~ 1300 km s $^{-1}$, there are three possible distances. If HI1232+20 were infalling from the near side, located at the center of the cluster, or infalling from the far side, it could have distances of ~ 12 , ~ 17 , or ~ 25 Mpc, respectively. Further complicating the nearby velocity field is the Coma I cloud just north of the HI1232+20 system. This complex of galaxies with peculiar velocities is centered around $(\alpha, \delta) = (12.5 \text{ hr}, +30^\circ)$ (Karachentsev et al. 2011). Still, we can make a crude but reliable estimate of the lower limit on the distance based on the fact that we do not resolve any individual stars in the optical counterpart of AGC 229385. WIYN has been used to successfully resolve stellar populations in galaxies under similar observing conditions out to 2–4 Mpc (e.g., Leo P; Rhode et al. 2013; M81 group; K. L. Rhode, private communication). Furthermore, WIYN observations of SHIELD galaxies (Cannon et al. 2011) resolve upper main sequence and supergiant stars at distance of 8 Mpc.

Many of the most extreme properties of the objects in the HI1232+20 system are distance-independent quantities and would not be affected by a more nearby distance (e.g., M_{HI}/L_B , surface brightness measurements and limits, average HI surface density). However, if they were only ~ 12 Mpc distant instead of 25 Mpc, the absolute quantities (e.g., HI mass, stellar mass, total luminosity, physical area) would all scale down by a factor of four. For example, the HI mass of AGC 229385 would

become $1.8 \times 10^8 M_\odot$, its stellar mass would be reduced to $3.8 \times 10^5 M_\odot$, its absolute B magnitude would be reduced to $M_B = -11.4$ mag, and its optical diameter would be ~ 2 kpc.

Even with the difficulties of constraining the absolute distance to the HI1232+20 system, we are interested in the large scale environment around it, and how isolated it has been on longer time scales. The background spiral galaxy AGC 222741 (CGCG 129-006, labeled in Figure 1) appears on the sky between the three sources in HI1232+20, but has a recession velocity of $v_{\text{lsr}} = 1884$ km s $^{-1}$, which is substantially higher than the velocities of the three sources in the system (1277, 1309, and 1348 km s $^{-1}$), so is very unlikely to be related. Figure 6 shows the galaxies in the area around these HI sources. Galaxies shown on the plot come from the Updated Zwicky Catalog (UZC; Falco et al. 1999), from the spectroscopic sample of SDSS DR9 (Ahn et al. 2012), and from the AGC. The UZC is an extragalactic redshift survey of $\sim 20,000$ galaxies that is 96% complete to $m_{\text{zw}} < 15.5$ mag and the SDSS DR9 spectroscopic survey includes spectra of ~ 1.5 million galaxies, and is 95% complete down to $r' = 17.7$ mag. On Figure 6, a red “x” indicates the location of the background spiral galaxy (AGC 222741), which appears near our HI sources on the sky. Also shown on Figure 6 is the projected virial radius of the northern subcluster of the Virgo Cluster of galaxies (Binggeli et al. 1985). The curves enclose a region centered at the position of M87 with a radius of $5^\circ.4$ and centered on a recession velocity of 1100 km s $^{-1}$ and extending 800 km s $^{-1}$ on either side (Ferrarese et al. 2012).

In order to demonstrate the complexity of the velocity field around HI1232+20, we calculate three-space separations between this system and any nearby sources, using only their positions and observed velocities. The three sources within the HI1232+20 system are all within $\sim 20'$ and ~ 70 km s $^{-1}$ of each other. While the global velocity field around these sources is complicated due to the influence of the nearby Virgo Cluster (Karachentsev & Nasonova 2010; Karachentsev et al. 2014), we use this approach to crudely identify any possible galaxies which may be near enough to affect this system, and have similar positions and velocities. The object with the most similar velocity and position is NGC 4561 with a velocity of 1360 km s $^{-1}$ and an angular separation of $1^\circ.4$, implying a physical separation of ~ 400 kpc assuming a simple Hubble flow. However, the Tully–Fisher distance to NGC 4561 is 12.3 Mpc (Tully & Fisher 1987), so it is likely infalling to the Virgo Cluster from the near side. The object with the next-smallest three-space distance is the starbursting galaxy IC 3605, which has a velocity of 1360 km s $^{-1}$ and is located $\sim 1^\circ.8$ to the SE, with an implied physical separation (Hubble flow only) of ~ 500 kpc. No other distance measurements exist for IC 3605. The locations of NGC 4561 and IC 3605 are indicated on Figure 6 with large dotted circles. The close proximity of this system to the Virgo Cluster means that its distance is uncertain and that the global velocity field is rich and complex.

4. DISCUSSION

The objects in the HI1232+20 system are not easily explained, and some of their properties seem contradictory and puzzling. For example, it is difficult to understand the star formation history of AGC 229385, which apparently has only produced a tiny population of stars in an otherwise massive HI cloud. The HI mass of AGC 229385 ($\log M_{\text{HI}} = 8.9$) is larger

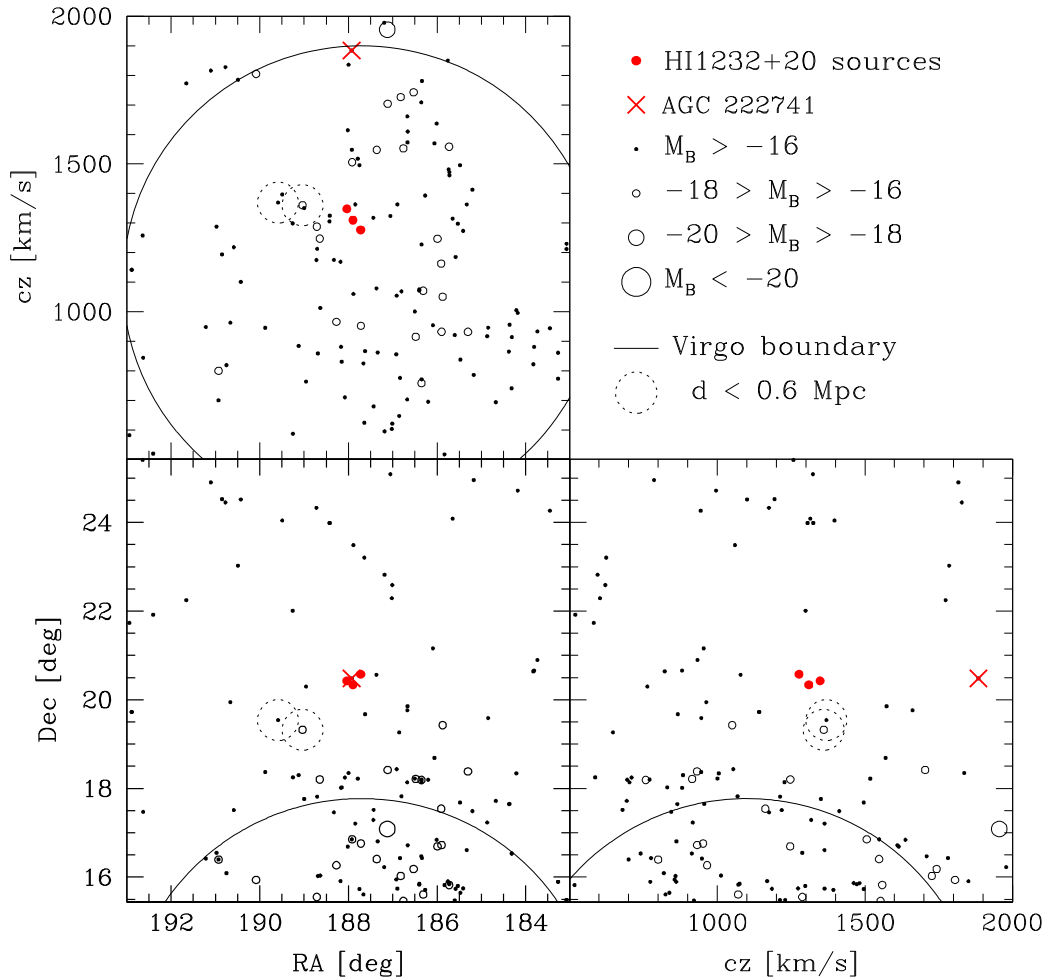


Figure 6. All panels show galaxies from the UZC, SDSS, and AGC. Larger circles represent more luminous galaxies, and smaller circles and dots represent less luminous galaxies. Note that we are plotting the three objects in the HI1232+20 system as red dots, as well as the background spiral galaxy (AGC 222741) at $cz = 1884 \text{ km s}^{-1}$ as a red “x.” The latter is near the objects in the HI1232+20 system on the sky, but is well-separated in the other two panels. The bottom left panel shows the galaxy distribution in the plane of the sky. The top left panel shows the galaxy distribution in the velocity–right ascension plane. The bottom right panel shows the galaxy distribution in the declination–velocity plane. The solid curved lines show the virial radius of the Virgo Cluster in each projection. Dotted circles enclose the galaxies nearest to this system.

than the nearby star-forming Large Magellanic Cloud ($\log M_{\text{HI}} = 8.7$; Kim et al. 1998) and just smaller than the nearby spiral galaxy M33 ($\log M_{\text{HI}} = 9.1$; Gratier et al. 2010), although its stellar populations and optical luminosity are vastly dissimilar. The HI kinematics of its HI cloud are also perplexing, as its rotation speed seems inadequate for its large mass and size. It is similarly difficult to explain why the other members of the HI1232+20 system have not formed any detectable stars, even with their substantial, although quite spread out, HI distributions. For comparison, both AGC229383 and AGC 229384 have larger HI masses than the nearby dI galaxies IC 10 and NGC 6822 ($\log M_{\text{HI}} = 8.0$; de Blok & Walter 2000; Nidever et al. 2013), but lack any optical counterparts in our observations.

In order to put these objects in context with other galaxies, we consider their locations in typical galaxy scaling relations. In this exercise, we are treating these objects as independent galaxies and not simply gas clouds that have been stripped or tidally disturbed. It is possible that objects like this may be part of a large but mostly-unobserved class of galaxies (e.g., the sunken galaxies of Disney 1976), but is more likely that the objects in this system are simply unique and uncommon

galaxies. Since AGC 229385 has an optical counterpart we consider its location on optical and HI scaling relations, while for the other sources our optical upper limits can still help constrain some of the same scaling relations. After discussing these scaling relations, we will consider some possible formation scenarios to explain this unusual system of objects.

4.1. M_{HI}/L Relationship

One of the most extreme properties of the objects in the HI1232+20 system is their exceptionally large HI mass-to-light ratio measurements (or lower limits). Galaxies are known to follow a typical relationship between this HI mass-to-light ratio and the overall luminosity. The HI mass-to-light ratio is defined as M_{HI}/L , where L is the optical luminosity, often measured in a blue filter. This relationship is especially difficult to measure for faint low-mass galaxies, where a significant fraction of the optical luminosity may come from LSB regions. Almost universally, whenever a galaxy with a reportedly large M_{HI}/L_B ratio is observed with deeper optical images, the ratio returns to more typical values near unity. Warren et al. (2004) used survey and catalog data to identify possible galaxies with a large M_{HI}/L_B ratio ($3 < M_{\text{HI}}/L_B < 27$), but their sample of 9

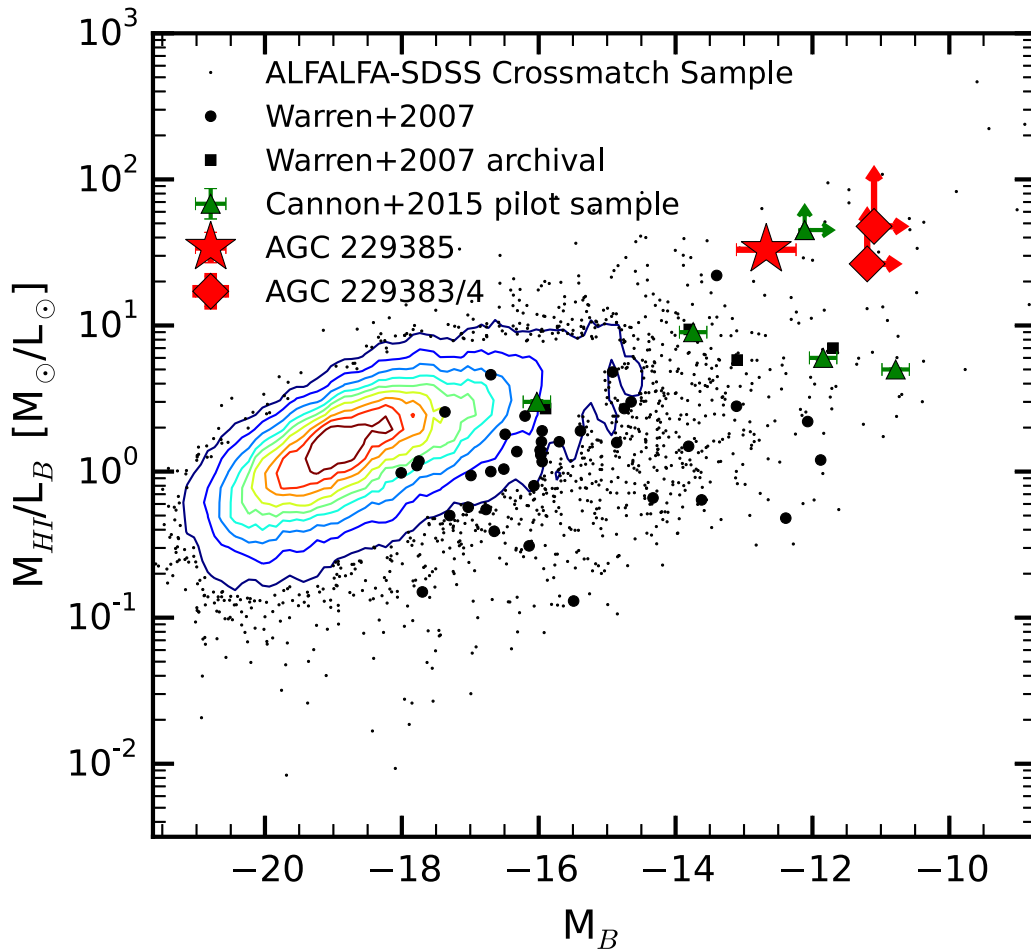


Figure 7. Relationship between the HI mass-to-light ratio (M_{HI}/L_B , in solar units) and absolute B magnitude. The small dots and contours indicate HI-detected galaxies from the ALFALFA $\alpha.40$ catalog matched with SDSS DR7 photometry. The dark circles and squares come from the new and archival observations of Warren et al. (2007). The green points show the five (almost) dark galaxies from the pilot observations of Cannon et al. (2015). AGC 229385 is shown as a red star, and the upper limits for AGC 229383 and AGC 229384 are indicated with diamond points and arrows. The error bars on AGC 229385 also include a distance uncertainty of ± 5 Mpc. The object from the Cannon et al. (2015) sample with a larger lower limit on M_{HI}/L_B than the measured value for AGC 229385 is AGC 208602 and is likely a tidal feature and not an isolated galaxy.

large M_{HI}/L_B galaxies were almost all found to have less extreme ratios ($M_{\text{HI}}/L_B < 5$) after deeper observations. Similarly, van Zee et al. (1997) used broadband optical imaging observations of six LSB dwarf galaxies to show that their catalogued optical magnitudes had been severely underestimated by ~ 1.5 mag, so their previously reported M_{HI}/L_B ratios became four times smaller and less extreme. Among dwarf galaxies, typical measurements of M_{HI}/L_B are between 0.15 and 4.2, considering a variety of samples including Sm/Im galaxies (Roberts & Haynes 1994; Stil & Israel 2002) and field dIs (Lee et al. 2003). The relatively small dynamic range of ratios (a factor of 30 between the lowest and highest ratio) highlights the importance of careful and accurate measurements of this ratio.

Figure 7 shows the relationship between the HI mass-to-light ratio (M_{HI}/L_B) and absolute B magnitude (M_B) for multiple samples of galaxies. The main dataset shown in Figure 7 comes from the matched ALFALFA $\alpha.40$ and SDSS catalogs of Haynes et al. (2011), which is the parent sample from which the ALFALFA (almost) dark galaxies are drawn. We note that the shallow SDSS photometry may underestimate the luminosity of the faint sources in this sample. The average exposure time in SDSS is only ~ 1 minute, and will not detect LSB

emission from these galaxies. Additionally, optical fluxes may be erroneously estimated due to issues with SDSS background subtraction and effects from nearby bright stars. Also shown on Figure 7 are galaxies from Warren et al. (2007), who observed 38 galaxies at optical and radio wavelengths, and also compiled an archival sample of previously observed galaxies. Some of these sources are observed at low Galactic latitude, which results in additional uncertainty in the necessary extinction corrections. The five (almost) dark galaxies from the pilot VLA observations of Cannon et al. (2015) are also shown on Figure 7 as green dots. The VLA observations allowed OCs to be identified for all but one of their sample, and the gas mass-to-light ratios for these sources are well-measured. We find that AGC 229385 has $M_{\text{HI}}/L_{g'} = 45.8 M_{\odot}/L_{\odot}$, or, converted to B via Jester et al. (2005), $M_{\text{HI}}/L_B = 38.2 M_{\odot}/L_{\odot}$, and its position is indicated on Figure 7. As AGC 229383 and AGC 229384 are not detected in our deep optical images, we can only determine lower limits on $M_{\text{HI}}/L_{g'}$, and find > 31 and $> 57 M_{\odot}/L_{\odot}$, respectively. These limits are also shown in Figure 7, where we have converted our upper limits in $M_{g'}$ to M_B assuming the same $g' - r'$ color as AGC 229385.

Warren et al. (2007) suggest that there is an upper envelope in Figure 7, which may represent the minimum amount of stars

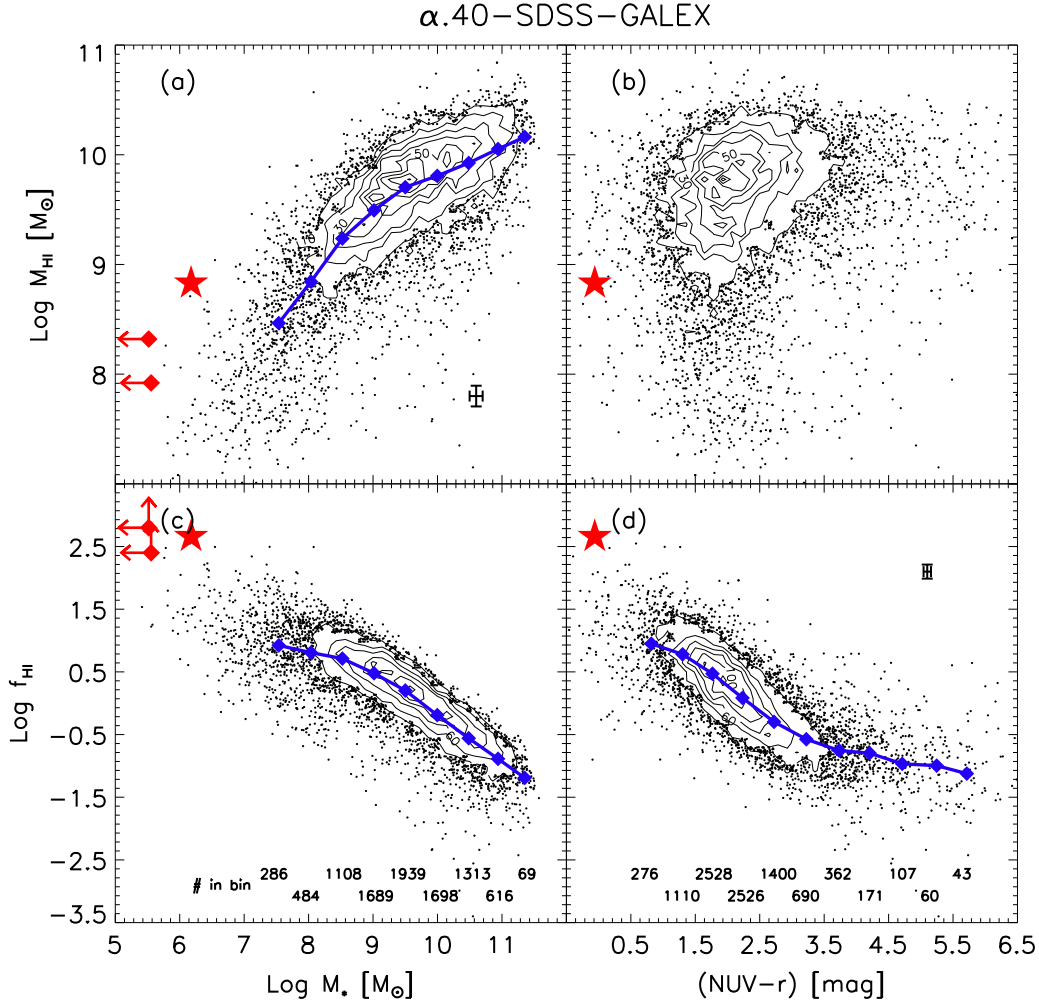


Figure 8. The scaling relations between HI and optical observations, using the $\alpha.40$ -SDSS-GALEX sample and analysis from Figure 8 of Huang et al. (2012b). In all panels, number densities of galaxies are calculated within grid cells set by the intervals of the minor ticks on the axes. Contours are drawn above densities of 20 galaxies per grid cell, and selected contours are labeled with their number densities. Blue diamonds and lines show the average y-values in each x-bin. Panel (a) shows the relationship between HI mass and stellar mass, with stellar masses from mass-to-light ratios from fits to SDSS photometry. Panel (b) shows the HI mass as a function of NUV- r color. Panel (c) shows the ratio of HI mass to stellar mass ($f_{\text{HI}} = M_{\text{HI}}/M_*$). Panel (d) shows the relationship between f_{HI} to NUV- r color. Typical error bars of individual galaxies are shown in the corner of panels (a) and (d). The red star shows the location of AGC 229385 in each panel, while the red arrows indicate the upper limits of AGC 229384 and AGC 229383 where measured.

a galaxy will form, given a shallow potential well and an isolated environment. The sources in the HI1232+20 system are in an extreme region of Figure 7, near this upper envelope. While there are other galaxies from ALFALFA with more extreme values of M_{HI}/L_B shown on the plot, none have ratios that are as well-determined as the objects in this system. SDSS photometry for faint LSB galaxies will likely underestimate their luminosity, which leads to an overestimate of the M_{HI}/L_B ratio. A recent study identified a low surface brightness galaxy near the Virgo Cluster with a very large HI mass-to-light ratio that they measure as $M_{\text{HI}}/L_V \gtrsim 20 M_\odot/L_\odot$ (Bellazzini et al. 2015). AGC229385 has the largest accurately measured HI mass-to-light ratio in the literature, but still appears to lie along a continuation of the trend seen in more luminous galaxies. Warren et al. (2007) use a similar sample of galaxies with HI and optical data to fit the relationship between M_{HI}/L_B and M_B . They fit the upper envelope of the relationship with the following expression:

$$\log(M_{\text{HI}}/L_B)_{\text{max}} = 0.19(M_B + 20.4).$$

For AGC 229385 its $M_B = -12.72$ would predict a maximum $M_{\text{HI}}/L_B = 29$. While AGC 229385 does follow the general

trend of low stellar mass objects having higher gas mass-to-light ratios, we measure $M_{\text{HI}}/L_B = 38$, which is even more extreme than the upper envelope of Warren et al. (2007).

4.2. Galaxy Scaling Relations with Stellar Mass

Studies of large samples of galaxies have found that stellar mass seems to be an important parameter that relates to star formation in the possible evolution of galaxies from the blue cloud to the red sequence (Brinchmann et al. 2004; Salim et al. 2007; Huang et al. 2012b). Using a sample of 9,417 ALFALFA-selected galaxies with counterparts in archival GALEX and SDSS images, Huang et al. (2012b) studied the scaling relations as a function of stellar mass and optical color (see their Figure 8). Figures 8(a) and (c) show the HI mass and $f_{\text{HI}} = M_{\text{HI}}/M_*$ as a function of the stellar mass, which is determined from SED fits. A clear relationship with M_{HI} is found from $M_* = 3.2 \times 10^7 M_\odot$ to $3.2 \times 10^{11} M_\odot$, with a change in slope at $M_* \sim 10^9 M_\odot$. Analogously, f_{HI} follows the same general trend with a break at $\sim 10^9 M_\odot$. On both panels the location of AGC 229385 is indicated with a large star, and the

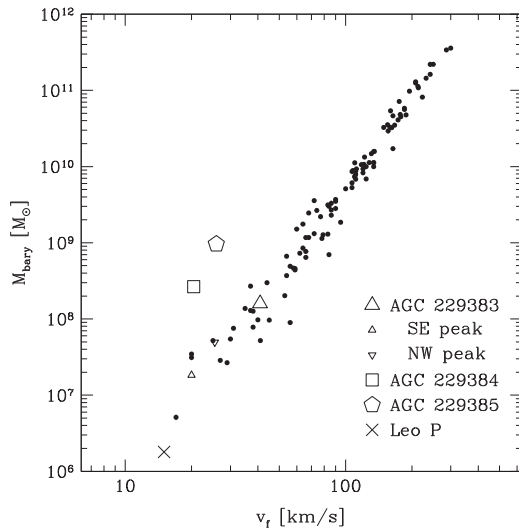


Figure 9. Baryonic Tully–Fisher relation. Black dots show galaxies measured by McGaugh (2005) and McGaugh (2012). Open polygons show the sources in the HI1232+20 system from this work. AGC 229385 (shown as an open pentagon) has the largest HI mass of this sample and is offset above the BTf relation. The next most massive, AGC 229384 (shown as an open square), is also offset above the relationship, while the least massive, AGC 229383 (shown as an open triangle), is consistent with the BTf relation. The two HI peaks of AGC 229383 are measured separately (shown as small triangles), and both lie along the BTf relation as well. The “x” shows the position of Leo P, a metal-poor gas-rich dwarf galaxy discovered by ALFALFA in the local volume just outside the Local Group (Giovannelli et al. 2013; Rhode et al. 2013; Bernstein-Cooper et al. 2014).

upper limit measurements of AGC 229383 and AGC 229384 are indicated with arrows. These sources are deviant from the expected scaling relations at the low stellar mass end, and have too much HI for their stellar mass (detected or not).

Figures 8(b) and (d) show M_{HI} and f_{HI} as a function of $\text{NUV} - r$ color, which acts as an indicator of the amount of recent star formation (UV) compared to the amount of past star formation (r). Here only AGC 229385 can be plotted, since we have no optical or UV detections of the other two sources. AGC 229385 is at an extreme location in both of these parameter spaces, and lies significantly above an extrapolation of the low mass trend in the relationship between f_{HI} and $\text{NUV} - r$. The color cannot be much bluer than it already is, since after 5 Myr, a simple stellar population of half solar metallicity will have $\text{NUV} - r = -0.2$ (Bressan et al. 2012). AGC 229385 seems to be deviant in the sense that it has too much HI for its $\text{NUV} - r$ color, consistent with the previously discussed panels. Finally, we note that Toribio et al. (2011) found a strong relationship between M_{HI} and the optical diameter measured at $\mu = 25 \text{ mag arcsec}^{-2}$, such that galaxies with smaller values D_{25} typically had smaller HI masses as well. However, we cannot compare the properties of the HI1232+20 system with this relationship because the optical counterpart to AGC 229385 never reaches $\mu = 25 \text{ mag arcsec}^{-2}$, and the other two sources have even fainter limits on their optical non-detections.

4.3. Galaxy Scaling Relations with HI Mass

We now discuss the scaling relations which depend on the total HI mass of a galaxy. First, we consider the relationship between HI diameter (measured at a particular the column density) and total HI mass. Broeils & Rhee (1997, hereafter BR97) observed this relationship in a sample of 108 spiral and

irregular galaxies and found a strong correlation between $\log M_{\text{HI}}$ and $\log D_{\text{HI}}$ (the HI diameter at $1 M_{\odot} \text{ pc}^{-2}$), with a dispersion of only 0.13 dex, and a slope of 1.96 ± 0.04 . Swaters et al. (2002) found the same correlation and slope when they used a sample of lower mass irregular galaxies. This relationship has been measured between HI masses of 6×10^7 and $3 \times 10^{10} M_{\odot}$ and between HI diameters of 0.8 and 160 kpc. A consistent relationship implies that there is a constant average HI density in all gas-rich galaxies, which BR97 estimated as $3.8 \pm 1.1 M_{\odot} \text{ pc}^{-2}$.

While explanations for the underlying mechanisms for this correlation are complex (e.g., feedback, turbulence, etc), it is simple to apply the relationship from BR97 to our sources. In the case of AGC 229385, our HI mass predicts an HI diameter of 16 kpc (measured at $1 M_{\odot} \text{ pc}^{-2}$). Our HI observations of AGC 229385 show an elongated source with dimensions $24 \times 10 \text{ kpc}$, when measured at this HI column density. This is $\sim 50\%$ larger than predicted, and while projection effects could reduce this discrepancy somewhat, the HI kinematics do not suggest we are viewing a disk edge-on so any correction for projection effects will be small. AGC 229384 has an HI mass of $2.00 \times 10^8 M_{\odot}$ which predicts an HI diameter of 8.1 kpc. Our observations show an elongated HI source with dimensions $10 \times 8 \text{ kpc}$, which is slightly larger than expected (although this source has two separate HI peaks at that column density). The HI distribution of AGC 229383 never reaches the column density that corresponds to $1 M_{\odot} \text{ pc}^{-2}$, and we are unable to apply this relationship to it. Both AGC 229385 and AGC 229384 have larger HI diameters than predicted by the HI diameter–HI mass scaling relation. This also implies that their average HI surface density is significantly less than the constant value found by BR97. Assuming a circular HI disk for AGC 229385 and AGC 229384, we find that their average HI surface densities are 1.6 and $2.4 M_{\odot} \text{ pc}^{-2}$, respectively, which are at the lower limit of the distribution found by BR97. Rosenberg & Schneider (2003) also compared M_{HI} and D_{HI} for a different sample, but their relationship gives similar results to BR97. These unusually low HI surface densities may be related to the lack of significant star formation in the objects in the HI1232+20 system.

4.4. Galaxy Scaling Relations with HI Kinematics

We consider the HI kinematics of the sources in the HI1232+20 system, especially with regard to their apparently slow rotation. However, since the HI rotation curves of these sources are difficult to fit or interpret (see Figures 3(e), 4(e), and 5(e)), we instead use the integrated width of the 21 cm line itself to measure their rotation. The HI velocity widths (W_{50} , measured at 50% of the peak value) of the three sources in the HI1232+20 system are unusually small for their HI masses. We model the HI velocity width distribution for all ALFALFA galaxies as a function of their HI mass. Integrating over the model distribution at the HI mass of AGC 229385 ($M_{\text{HI}} = 6.7 \times 10^8 M_{\odot}$) we find that only 2% of ALFALFA galaxies have velocity widths smaller than its measured value of $W_{50} = 34 \text{ km s}^{-1}$. Similarly for AGC 229384, we find only 3% of ALFALFA galaxies at its HI mass have similarly small values of W_{50} . We note that the much wider velocity width of AGC 229383 falls near the 50th percentile of objects of its HI mass, but that this may be due to the presence of multiple objects within the ALFALFA beam. Full details of the velocity

width model will be published in a forthcoming paper (M. Jones et al. 2015, in preparation).

We can next use the baryonic Tully–Fisher relation (McGaugh 2012) to compare the total baryonic masses with the rotation velocities for the members of the HI1232+20 system. Since these objects are gas-dominated, we use the relationship from McGaugh (2012) to calculate rotation velocities as $v_f = W_{20}/2$, where W_{20} is the HI velocity width at 20% of the maximum. While the HI rotation of these objects is difficult to measure accurately, their placement on the BTF relation is intended as a suggestive exercise to shed light on some of their unusual properties. If these objects are indeed galaxies, then their rotation seems too slow for their measured mass.

Figure 9 shows the locations of the objects in the HI1232+20 system compared to a large sample of galaxies (McGaugh 2005, 2012). The baryonic mass is the sum of the stellar and total gas mass, and in gas-dominated galaxies without substantial stellar populations, is determined as $M_{\text{bary}} = 1.33 \times M_{\text{HI}}$, where the extra factor of 1.33 accounts for helium. The stellar mass of the optical counterpart of AGC229385 contributes only a negligible $\sim 0.2\%$ compared to its HI mass. The upper limits on the non-detections of stellar populations of the other two objects indicate that these would contribute similarly negligible amounts of baryonic mass. This estimate of baryonic mass does not include contributions from molecular or ionized gas. It is conceivable that there may be an envelope of low density ionized gas surrounding these galaxies, contributing more mass than is included in our determination of M_{bary} .

Figure 9 shows that the two more massive objects in the HI1232+20 system both fall significantly above the standard BTF relationship, while the least massive (AGC 229383) is in agreement. However, since AGC 229383 has two strong HI peaks which are separated by ~ 40 kpc, we also consider the kinematics of each clump separately, and plot them on Figure 9 as well. AGC 229383 is the lowest column density object of this system, and is, at best, difficult to interpret. Naïve placement of the combined object or its peaks seems to agree reasonably well with the BTF, but the low signal-to-noise nature of the HI observations makes further analysis or interpretation difficult. We also caution that the WSRT observations do not recover the total HI flux of ALFALFA (see Section 3.3), so the HI masses of the two peaks do not sum to the total observed mass.

We note that inclination effects could slightly modify our determination of rotation velocities, but that the discrepancies from the BTF are larger than can be accounted for by changing the inclination angle of the objects. If the distance to the HI1232+20 system was significantly smaller, then they would be in better agreement with the BTF. In order for AGC 229385 to agree with the BTF it would need to be at a distance of ~ 4.4 Mpc, and AGC 229384 would need to be at a distance of ~ 5.4 Mpc. This smaller distance is unlikely given other constraints (e.g., the lack of resolved stars in our optical observations, see Section 3.4.2).

We also consider the ratio of dynamical mass to HI mass ($M_{\text{dyn}}/M_{\text{HI}}$) as another independent constraint on the distance by assuming a typical value of $M_{\text{dyn}}/M_{\text{HI}} = 10$. We measure an effective velocity ($v_{\text{eff}}^2 = v_{\text{rot}}^2 + 3\sigma_v^2$) for AGC 229385 of $v_{\text{eff}} = 21.2 \text{ km s}^{-1}$, so this relationship implies a distance of 4.3 Mpc. If we assume no dark matter (e.g., $M_{\text{dyn}}/M_{\text{HI}} = 1.3$), we find a

distance of 32.8 Mpc instead. The HI kinematics of AGC 229384 and AGC 229383 make it difficult to measure v_{rot} , which is required to determine v_{eff} .

4.5. Formation Scenarios

Given the variety of observational constraints we have for the sources in the HI1232+20 system, and the context from existing galaxy scaling relations, we now consider some of the possible evolutionary scenarios which could account for a system like this.

The blue color of the optical counterpart of AGC 229385 suggests that it may consist of a mostly young stellar population. If this object has only just begun forming stars, it may not have had enough time yet to convert a significant amount of its gas into stars, as reflected by the high gas mass-to-light ratio. However, the lack of $H\alpha$ detection and the weak UV SFR ($\sim 0.004 M_{\odot} \text{ yr}^{-1}$) seem to indicate that it is only slowly forming stars. At this rate it would take more than a Hubble time to generate enough mass in stars to return it to the normal relationship between HI and stellar mass (e.g., Figure 8(a)).

It is difficult to find a single convincing explanation for why one HI cloud has an observable stellar population while its two nearby neighbors do not. Obviously, this creates a “fine-tuning” problem of sorts. Interactions between the members of this system may have triggered star formation in the most massive object. It is also possible that the system may have been perturbed by an external object. Our analysis in Section 3.4.1 showed that there was only one plausible perturber nearby, even given our generous assumptions about relative velocities and timescales for interactions.

Alternatively, Verde et al. (2002) have suggested that low-mass dark matter halos can contain neutral gas without ever forming stars, under certain conditions. However, the members of this system have substantial HI masses and are likely different from the low-mass dark matter halos of Verde et al. (2002). It may be that star formation has only occurred in the HI cloud which is dense enough at its center to exceed a gas density threshold (e.g., Kennicutt 1998). Indeed, in studies of the outer disks of larger galaxies, star formation appears to cease below an HI surface density of $\sim 1 M_{\odot} \text{ pc}^{-2}$ (Radburn-Smith et al. 2012; Hunter et al. 2013). The HI distributions of the sources in the HI1232+20 system are mostly below this surface density threshold, and only the peak of AGC 229385 substantially exceeds it.

The reasons behind the low gas surface density and over-extended HI distributions of these objects are not clear. In the case of AGC 229385 it is possible that feedback from the star formation (perhaps stronger in the past) has injected kinetic energy into the HI, and temporarily expanded it. Or we may be seeing the results of a recent infall of cold gas into this system. However, these objects have significant amounts of HI, and it is difficult to justify an inflow scenario which could provide enough gas while maintaining a low gas density and inhibit star formation.

It is also possible that these objects may be the most massive knots in a system of smaller HI clouds which are in the midst of a tidal interaction or merger event. AGC 229385 and AGC 229384 may be the brightest HI peaks, and could be the products of recent mergers of smaller HI clumps. The extended nature of AGC 229383 and its two HI peaks are suggestive of an extended HI distribution with local peaks and

clumps. However, the ALFALFA observations are very sensitive to faint HI emission, and given the good agreement between WSRT and ALFALFA HI fluxes for AGC 229385 and AGC 229384, it seems unlikely that there is a substantial amount of unseen extended gas in most of the system.

The HI1232+20 system does not seem to be a tidal feature or remnant of a larger object, based on the lack of a clear connection to any possible external perturbing object. However, tidal interactions between members of the system may be important to their individual star formation histories. The HI clouds in this system have extremely low star formation efficiencies and low gas densities. These low gas densities are especially difficult to reconcile with the significant HI masses of these sources. The HI mass of AGC 229385 is greater than that of the LMC, and AGC 229383 has more HI than some nearby star-forming dwarf irregular galaxies. Even if recent tidal interactions between the sources may have triggered a burst of star formation in AGC 229385, the overall properties of the HI1232+20 system are difficult to convincingly interpret and explain.

5. SUMMARY

In this work we present the discovery of the HI1232+20 system of HI sources, drawn from the sample of (almost) dark extragalactic sources in ALFALFA. This system defies conventional explanations and our HI synthesis imaging and deep optical observations have revealed a set of objects with properties that are difficult to reconcile with typical scaling relations. The most massive of its members (AGC 229385, $M_{\text{HI}} = 7.2 \times 10^8 M_{\odot}$) has a weak stellar counterpart, detected in UV and ultra-deep optical imaging, with a peak surface brightness of $\mu_{g'} = 26.4 \text{ mag arcsec}^{-2}$. It has the most extreme well-measured gas mass-to-light ratio in the literature ($M_{\text{HI}}/L_B = 38$), and its absolute magnitude is only $M_{g'} = -12.9 \text{ mag}$ ($M_{\star} = 1.5 \times 10^6 M_{\odot}$), assuming a distance of 25 Mpc. We do not detect optical counterparts for the other two members, but place upper limits on their absolute magnitudes of $M_{g'} > -11.3 \text{ mag}$ ($M_{\star} < 3 \times 10^5 M_{\odot}$). The HI kinematics of the three objects in this system are inconsistent with typical galaxy scaling relations, with HI distributions that are too extended and too slowly rotating for their HI mass. This group appears on the sky just outside of the projected virial radius of the Virgo Cluster, but is otherwise isolated from any nearby galaxies.

The HI1232+20 system is difficult to explain completely, but may be an example of objects just above and just below a threshold for star formation. The most massive of the three sources is forming stars, but may have only recently started to do so. The other two sources have no observational signatures of star formation, so there may be some mechanism inhibiting this process. Sources like these are very rare in the ALFALFA survey, especially at such large HI masses. As observations of the HI1232+20 system continue we hope to learn more about its history and role in galaxy formation and evolution.

We thank the entire ALFALFA team for their efforts in observing and data processing that produced the ALFALFA source catalog. We also thank S. Huang for providing the data shown in Figure 8, from Huang et al. (2012b). We thank the anonymous referee for very helpful feedback and comments which have improved this work. The ALFALFA work at

Cornell is supported by NSF grants AST-0607007 and AST-1107390 to R.G. and M.P.H. and by grants from the Brinson Foundation. J.M.C. is supported by NSF grant 1211683. K.L.R. & W.F.J. are supported by NSF Early Career Development Award AST-0847109. This research has made extensive use of the invaluable NASA/IPAC Extragalactic Database (NED) which is operated by the Jet Propulsion Laboratory, California Institute of Technology, under contract with the National Aeronautics and Space Administration. This research has also made use of NASA's Astrophysics Data System.

REFERENCES

- Ahn, C. P., Alexandroff, R., Allende Prieto, C., et al. 2012, *ApJS*, **203**, 21
 Bellazzini, M., Magrini, L., Mucciarelli, A., et al. 2015, *ApJL*, **800**, L15
 Bernstein-Cooper, E. Z., Cannon, J. M., Elson, E. C., et al. 2014, *AJ*, **148**, 35
 Bianchi, L., Conti, A., & Shiao, B. 2014, *AdSpR*, **53**, 900
 Binggeli, B., Sandage, A., & Tammann, G. A. 1985, *AJ*, **90**, 1681
 Bressan, A., Marigo, P., Girardi, L., et al. 2012, *MNRAS*, **427**, 127
 Brinchmann, J., Charlot, S., White, S. D. M., et al. 1995, *MNRAS*, **351**, 1151
 Broeils, A. H., & Rhee, M.-H. 1997, *A&A*, **324**, 877
 Cannon, J. M., Giovanelli, R., Haynes, M. P., et al. 2011, *ApJL*, **739**, L22
 Cannon, J. M., Martinkus, C. P., Leisman, L., et al. 2015, *AJ*, **149**, 72
 Chengalur, J. N., Giovanelli, R., & Haynes, M. P. 1995, *AJ*, **109**, 2415
 de Blok, W. J. G., & Walter, F. 2000, in ASP Conf. Ser. 218, Mapping the Hidden Universe: The Universe behind the Milky Way—The Universe in HI, ed. R. C. Kraan-Korteweg, P. A. Henning, & H. Andemach (San Francisco, CA: ASP), 218
 Disney, M. J. 1976, *Natur*, **263**, 573
 Doi, M., Tanaka, M., Fukugita, M., et al. 2010, *AJ*, **139**, 1628
 Doyle, M. T., Drinkwater, M. J., Rohde, D. J., et al. 2005, *MNRAS*, **361**, 34
 Duc, P.-A., & Bouchaud, F. 2008, *ApJ*, **673**, 787
 Dutton, A. A., van den Bosch, F. C., Dekel, A., & Courteau, S. 2007, *ApJ*, **654**, 27
 van Eymeren, J., Marcelin, M., Koribalski, B. S., et al. 2009, *A&A*, **505**, 105
 Falco, E. E., Kurtz, M. J., Geller, M. J., et al. 1999, *PASP*, **111**, 438
 Ferrarese, L., Côté, P., Cuillandre, J.-C., et al. 2012, *ApJS*, **200**, 4
 Geha, M., Blanton, M. R., Masjedi, M., & West, A. A. 2006, *ApJ*, **653**, 240
 Giovanelli, R., Haynes, M. P., Kent, B. R., et al. 2005, *AJ*, **130**, 2598
 Giovanelli, R., Haynes, M. P., Adams, E. A. K., et al. 2013, *AJ*, **146**, 15
 Gopu, A., Hayashi, S., & Young, M. D. 2014, in ASP Conf. Ser. 485, Astronomical Data Analysis Software and Systems XXIII, ed. N. Manset & P. Forshaw (San Francisco, CA: ASP), 485
 Gratier, P., Braine, J., Rodriguez-Fernandez, N. J., et al. 2010, *A&A*, **522**, AA3
 Gunn, J. E., Carr, M., Rockosi, C., et al. 1998, *AJ*, **116**, 3040
 Hao, C.-N., Kennicutt, R. C., Johnson, B. D., et al. 2011, *ApJ*, **741**, 124
 Haynes, M. P., Giovanelli, R., Martin, A. M., et al. 2011, *AJ*, **142**, 170
 Hopkins, A. M., & Beacom, J. F. 2006, *ApJ*, **651**, 142
 Huang, S., Haynes, M. P., Giovanelli, R., et al. 2012a, *AJ*, **143**, 133
 Huang, S., Haynes, M. P., Giovanelli, R., & Brinchmann, J. 2012b, *ApJ*, **756**, 113
 Hunter, D. A., Elmegreen, B. G., Rubin, V. C., et al. 2013, *AJ*, **146**, 92
 Jester, S., Schneider, D. P., Richards, G. T., et al. 2005, *AJ*, **130**, 873
 Karachentsev, I. D., & Nasonova, O. G. 2010, *MNRAS*, **405**, 1075
 Karachentsev, I. D., Nasonova, O. G., & Courtois, H. M. 2011, *ApJ*, **743**, 123
 Karachentsev, I. D., Tully, R. B., Wu, P.-F., Shaya, E. J., & Dolphin, A. E. 2014, *ApJ*, **782**, 4
 Kennicutt, R. C., Jr. 1998, *ApJ*, **498**, 541
 Kim, S., Staveley-Smith, L., Dopita, M. A., et al. 1998, *ApJ*, **503**, 674
 Kotulla, R. 2014, in ASP Conf. Ser. 485, Astronomical Data Analysis Software and Systems XXIII, ed. N. Manset & P. Forshaw (San Francisco, CA: ASP), 485
 Lee, H., McCall, M. L., Kingsburgh, R. L., Ross, R., & Stevenson, C. C. 2003, *AJ*, **125**, 146
 Lelli, F., Fraternali, F., & Sancisi, R. 2010, *A&A*, **516**, AA11
 Lucy, L. B. 1974, *AJ*, **79**, 745
 Madau, P., Pozzetti, L., & Dickinson, M. 1998, *ApJ*, **498**, 106
 Martin, D. C., Fanson, J., Schiminovich, D., et al. 2005, *ApJL*, **619**, L1
 Martin, A. M., Giovanelli, R., Haynes, M. P., et al. 2009, *ApJS*, **183**, 214
 Martin, A. M., Papastergis, E., Giovanelli, R., et al. 2010, *ApJ*, **723**, 1359
 Masters, K. L. 2005, PhD thesis, Cornell Univ.
 Matsuoka, Y., Ienaka, N., Oyabu, S., Wada, K., & Takino, S. 2012, *AJ*, **144**, 159

- McGaugh, S. S., Schombert, J. M., Bothun, G. D., & de Blok, W. J. G. 2000, *ApJL*, **533**, L99
- McGaugh, S. S. 2005, *ApJ*, **632**, 859
- McGaugh, S. S. 2012, *AJ*, **143**, 40
- McGaugh, S. S., & de Blok, W. J. G. 1997, *ApJ*, **481**, 689
- McGaugh, S. S., & Schombert, J. M. 2014, *AJ*, **148**, 77
- Morrissey, P., Conrow, T., Barlow, T. A., et al. 2007, *ApJS*, **173**, 682
- Murphy, E. J., Condon, J. J., Schinnerer, E., et al. 2011, *ApJ*, **737**, 67
- Nidever, D. L., Ashley, T., Slater, C. T., et al. 2013, *ApJL*, **779**, LL15
- Radburn-Smith, D. J., Roškar, R., Debattista, V. P., et al. 2012, *ApJ*, **753**, 138
- Rhode, K. L., Salzer, J. J., Haurberg, N. C., et al. 2013, *AJ*, **145**, 149
- Roberts, M. S., & Haynes, M. P. 1994, *ARA&A*, **32**, 115
- Rosenberg, J. L., & Schneider, S. E. 2003, *ApJ*, **585**, 256
- Rudick, C. S., Mihos, J. C., Harding, P., et al. 2010, *ApJ*, **720**, 569
- Saintonge, A. 2007, *AJ*, **133**, 2087
- Salim, S., Rich, R. M., Charlot, S., et al. 2007, *ApJS*, **173**, 267
- Sancisi, R., Broeils, A., Kamphuis, J., & van der Hulst, T. 1990, *Int. Conf. on Dynamics and Interactions of Galaxies* (Berlin: Springer), 304
- Sandage, A. 1976, *AJ*, **81**, 954
- Sault, R. J., Teuben, P. J., & Wright, M. C. H. 1995, *Astronomical Data Analysis Software and Systems IV*, 77
- Schlafly, E. F., & Finkbeiner, D. P. 2011, *ApJ*, **737**, 103
- Schlegel, D. J., Finkbeiner, D. P., & Davis, M. 1998, *ApJ*, **500**, 525
- Schombert, J., Maciel, T., & McGaugh, S. 2011, *AdAst*, **2011**, 143698
- Schombert, J., & McGaugh, S. 2014, *PASA*, **31**, e036
- Serra, P., Oosterloo, T., Morganti, R., et al. 2012, *MNRAS*, **422**, 1835
- Stil, J. M., & Israel, F. P. 2002, *A&A*, **389**, 29
- Swaters, R. A., van Albada, T. S., van der Hulst, J. M., & Sancisi, R. 2002, *A&A*, **390**, 829
- Taylor, E. N., & Webster, R. L. 2005, *ApJ*, **634**, 1067
- Toribio, M. C., Solanes, J. M., Giovanelli, R., Haynes, M. P., & Martin, A. M. 2011, *ApJ*, **732**, 93
- Tully, R. B., & Fisher, J. R. 1977, *A&A*, **54**, 661
- Tully, R. B., & Fisher, J. R. 1987, *Atlas of Nearby Galaxies* (Cambridge: Cambridge Univ. Press)
- van Zee, L., Haynes, M. P., Salzer, J. J., & Broeils, A. H. 1997, *AJ*, **113**, 1618
- Verde, L., Oh, S. P., & Jimenez, R. 2002, *MNRAS*, **336**, 541
- Wang, J., Kauffmann, G., Józsa, G. I. G., et al. 2013, *MNRAS*, **433**, 270
- Warmels, R. H. 1988, *A&As*, **72**, 427
- Warren, B. E., Jerjen, H., & Koribalski, B. S. 2007, *AJ*, **134**, 1849
- Warren, B. E., Jerjen, H., & Koribalski, B. S. 2004, *AJ*, **128**, 1152
- Williams, R. E., Blacker, B., Dickinson, M., et al. 1996, *AJ*, **112**, 1335
- Witt, A. N., Mandel, S., Sell, P. H., Dixon, T., & Vihj, U. P. 2008, *ApJ*, **679**, 497
- Wright, E. L., Eisenhardt, P. R. M., Mainzer, A. K., et al. 2010, *AJ*, **140**, 1868
- Young, M. D., Gopu, A., Hayashi, S., & Cox, J. A. 2013, in *ASP Conf. Ser. 475, Astronomical Data Analysis Software and Systems XXII*, ed. D. N. Friedel (San Francisco, CA: ASP), 475